J. Fluid Mech. (2013), *vol.* 730, *pp.* 19–51.
doi:10.1017/jfm.2013.272

Unsteady separation leading to secondary and tertiary vortex dynamics: the sub-α- and sub-β-phenomena

Jiten C. Kalita[1,†] **and Shuvam Sen**[2]

[1]Department of Mathematics, Indian Institute of Technology Guwahati, Guwahati 781039, India
[2]Department of Mathematical Sciences, Tezpur University, Tezpur 784028, India

(Received 22 May 2012; revised 18 March 2013; accepted 27 May 2013;
first published online 30 July 2013)

Studies on the α- and β-phenomena, terms coined by Bouard & Coutanceau (*J. Fluid Mech.*, vol. 101, 1980, pp. 583–607) for the flow past an impulsively started circular cylinder, have been confined only to the very early stages of the flow. In this paper, besides making a comprehensive in-depth analysis of these phenomena for a much longer period of time, we report the existence of some tertiary vortex phenomena for the first time, which we term the sub-α- and sub-β-phenomena. The mechanism of unsteady flow separation at high Reynolds numbers for the flow past a circular cylinder developed in the last two decades has been used to understand these flow phenomena. The flow is computed using a recently developed compact finite difference method for the biharmonic form of the two-dimensional Navier–Stokes equations for the range of Reynolds number $500 \leqslant Re \leqslant 10\,000$. We specifically choose $Re = 5000$ to describe the interplay among the primary, secondary and tertiary vortices leading to these interesting vortex dynamics. We also report a β-like phenomenon which is very similar to the β-phenomenon, but slightly differs in details. We offer a new perception of the α-phenomenon by defining its existence in a strong and weak sense along with a clearer characterization of the β-phenomenon. Apart from numerical computation, a detailed theoretical characterization using topological aspects of the boundary layer separation leading to the secondary and tertiary vortex phenomena has also been carried out. We compare our numerical results with established experimental and numerical results wherever available and an excellent match with the experimental results is obtained in all cases.

Key words: aerodynamics, computational methods, flow–structure interactions, mathematical foundations, Navier–Stokes equations

1. Introduction

The flow past an impulsively started circular cylinder has caught the attention of the fluid dynamics community for well over a century because of its intriguing physics and wide range of practical applications. It is well known that for high Reynolds numbers, flow separation for this problem takes place at a very early stage. With the appearance of secondary and subsequent tertiary vortices the flow field in the

† Email address for correspondence: jiten@iitg.ernet.in

vicinity of the solid surface gives rise to complex, intriguing structures with fascinating interplay between them. One such set of remarkable structures can be seen during the α- and β-phenomena, the origin of which dates back to the laboratory experiments of Bouard & Coutanceau (1980). Though they mention the computation of Thoman & Szewczyk (1969) giving an indication of the α-phenomenon in their work back in the late 1960s, the term was first coined by Bouard & Coutanceau (1980) after nearly a decade later. Notwithstanding their existence over the last three decades, very little in-depth analysis of these two phenomena is available in the literature.

Flow past a circular cylinder for $Re \geqslant 6$ is known for the formation of two symmetric vortices behind the cylinder almost immediately after the impulsive start. These vortices are stronger and larger for higher Re. For $47 < Re < 190$ the flow is essentially two-dimensional and is characterized by the formation of a regular von Kármán vortex street in the wake. With an increase in Re the flow becomes three-dimensional and the advent of various modes of instabilities drives the turbulent transition point upward. It is well documented that depending on the laboratory setup, for $Re \in [400, 2 \times 10^5]$, after an initial duration of laminar flow, transition to turbulence proceeds toward the direction of the circular cylinder and takes place in the shear layers. However, Kelvin–Helmholtz instability of separated shear layers is considered to be essentially two-dimensional and the transition of the boundary layer flow to turbulence begins only at $Re = 2 \times 10^5$ (Singh & Mittal 2004). One of the aims of this work is to capture the underlying mechanism of unsteady separation in the shear layer and explain some interesting hitherto unreported phenomena related to the formation of secondary and tertiary vortices.

There are several experimental and numerical studies that indicate the existence of the α-phenomenon in the range $800 \leqslant Re \leqslant 5000$ during the early stages of the flow (see Bouard & Coutanceau 1980; Loc 1980; Coutanceau & Defaye 1991). For this range of Re, when the primary vortex is still stable, as time progresses, the streamlines close to the cylinder initially deviate from the surface causing a bulge pattern eventually giving rise to a secondary eddy. This eddy grows in size to such an extent that it touches the boundary of the main eddy, thereby splitting the main one into two parts and isolating the region of the wake next to the separation point where another secondary eddy becomes visible. In the words of Bouard & Coutanceau (1980) 'these two secondary eddies are equivalent in size and strength and constitute a pair of secondary eddies'. This is what is known as the α-phenomenon, which is clearly evident for $Re = 3000$ at time $t = 2.5$ as shown in figure 1(a). On the other hand, for certain Reynolds numbers, just after the start of the flow, a very thin recirculating wake is formed; but soon afterwards, the core of this recirculating zone rotates in one piece with a speed which is much faster than the other part of the separated zone, forming a vortex which gains strength and size with time. After a while, this vortex separates the initial wake into two parts where the one situated near the point of separation is occupied by a pair of secondary eddies. This phenomenon is clearly exemplified by the flow patterns for $Re = 9500$ at time $t = 1.0$ depicted in figure 1(b).

Over the years, both these phenomena have been numerically validated by several studies. However, almost all of them are confined to the study of the α-phenomenon for Reynolds numbers 3000 and the β-phenomenon for 9500. Moreover all of them (Loc 1980; Loc & Bouard 1985; Chang & Chern 1991; Sengupta & Sengupta 1994; Chou & Huang 1996; Sanyasiraju & Manjula 2005; Kalita & Ray 2009) were limited to only a few snapshots of the secondary vortices at certain times without discussing the evolution of the vortices at length. Also, detailed analysis of successive occurrences of these two phenomena one after another which is typical of certain high

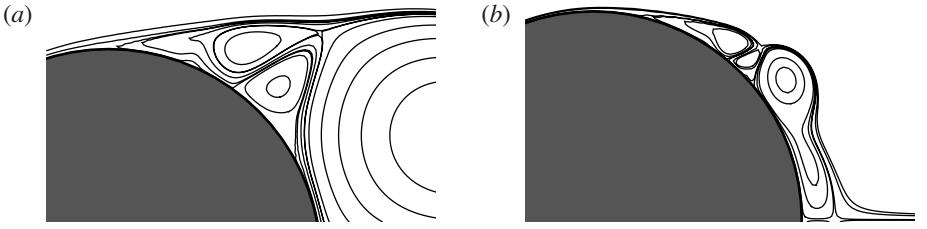

FIGURE 1. (*a*) The α-phenomenon (for $Re = 3000$ at time $t = 2.5$) and (*b*) the β-phenomenon ($Re = 9500$ at time $t = 1.0$): the streamlines are generated from our own computation.

Reynolds numbers has failed to catch the attention of the computational fluid dynamics community. Note that despite being in the laminar regime, the region of occurrence of these phenomena is rich in vortex structures and is rapidly changing. The evidence of this can be gauged from the surface vorticity distribution which contains several peaks and troughs of local maxima and minima. Although Koumoutsakos & Leonard (1995) indicated the presence of some tertiary vortex phenomena for $Re = 3000$ and 9500, to the best of our knowledge, there has been no detailed discussion on the formation and development of vortices beyond the secondary level. Note that the strength and size of these vortices being very small, accurately collecting data on these structures through experimental visualization is also tricky.

Earlier experimental studies by Coutanceau for $Re = 4500$ (Coutanceau & Defaye 1991) and for $Re = 5000$ (Bouard & Coutanceau 1980) clearly show that the α-phenomenon is preceded by the β-phenomenon for $Re = 4500$ and 5000. Note that though one can witness the presence of the β-phenomenon in the experimental visualization of Bouard & Coutanceau (1980) for $Re = 9500$ for the very early stages of the flow, no further information was available for the remainder of the flow. Likewise, the experimental visualization of Coutanceau & Defaye (1991) for $Re = 10\,000$ was inconclusive on the occurrence of the α-phenomenon following the β-phenomenon. Bouard & Coutanceau (1980) mention some indication of the α-phenomenon for Reynolds number as high as 40 000 in the numerical work of Thoman & Szewczyk (1969). However, the streamlines plotted by them did not provide enough evidence for such a conclusion; the same can be said about the simulation of Chou & Huang (1996) for the same *Re*. In the same vein, Chang & Chern (1991) claimed the existence of the α-phenomenon in their simulation for $Re = 9500$, 20 000 and 10^5 without their numerical visualization substantiating this. The shroud over the existence of the α-phenomenon in the early stages of the flow for higher *Re* was due to the fact that the studies mentioned above did not provide any data that can prove the closeness of the strength of the vortices constituting this phenomenon.

The formation of the recirculation zones leading to the phenomena described above is preceded by separation on the surface of the cylinder and is directly associated with the spontaneous generation of a singularity in the solution of governing equations in the boundary layer. This issue was settled in the early 1980s (Dommelen & Shen 1980) which led to extensive use of numerical techniques later on for Navier–Stokes equations in order to characterize the process of unsteady separation in the viscous incompressible flow past a solid wall. Numerical methods have been used to explain the abrupt eruption of boundary layers associated with unsteady flows at high *Re*.

In one of the pioneering works using boundary layer interaction, Sarpkaya & Schoafft (1979) presented and compared characteristics of various flow properties along with that of a vortex street. Applying numerical techniques, Peridier, Smith & Walker (1991) concluded that in the case of a plane wall, the adverse pressure gradient due to the vortex leads to the development of a recirculation zone in the viscous flow in the vicinity of a surface. In such a situation the boundary-layer flow focuses rapidly toward an eruption along a band which is very narrow in the streamwise direction. The authors also concluded that the solution in the boundary layer develops a separation singularity and evolves towards a terminal stage which is generic in two-dimensional unsteady flows. Later Cassel, Smith & Walker (1996) demonstrated that prior to this singularity the flow in the vicinity of the separation point becomes unstable at the onset of interaction with the external inviscid flow and argued that this instability should also be present within conventional unsteady interacting boundary layers. A detailed study of abrupt eruption of the boundary layers at high Re for flow past a circular cylinder was carried out by Koumoutsakos & Leonard (1995). They provided insight into the interactions between vortical structures and a wall, and identified the underlying mechanism for drag change. The authors captured with remarkable accuracy the square-root singularity as depicted by the drag coefficient at the very onset of the flow. But their computations differ from the experimental results at later times and have not been able to capture tertiary vortices, which may be attributed to the inherent problem that the vortex methods have in dealing with diffusion and the no-slip boundary condition. Numerical solutions of the Navier–Stokes (N–S) equations show that in the flow regime such as $Re = 10^4$, the locally thickening boundary layer in the vicinity of the eruption provokes a two-stage interaction between the viscous boundary layer and the outer inviscid flow (Obabko & Cassel 2002). The flow here experiences a large-scale interaction followed by a small-scale interaction due to spike formation. Obabko & Cassel (2002) have concluded that the large-scale interaction controls the overall evolution of unsteady separation and splits the primary eddy into multiple corotating eddies which later merge together before being lifted away. Note that splitting of the primary eddy into multiple corotating eddies for $Re = 9500$ has been observed in the experimental study of Bouard & Coutanceau (1980) and was termed the β-phenomenon for flow past a circular cylinder.

It is well known that a topological classification provides guidelines for identification of structures in any flow. Bifurcations near a critical point on a stationary plane based on topological considerations were studied by Bakker (1989). Ma & Wang (2002) presented a survey of a new dynamical systems theory pertaining to the topology of two-dimensional incompressible flows and its application to geophysical fluid dynamics. This was followed by a detailed theoretical study of the streamline topologies close to a solid wall for incompressible viscous flows by Ghil *et al.* (2004) and Ghil, Ma & Wang (2005). Using the boundary layer separation theory based on the structural bifurcation concept, they showed that structural bifurcation occurs whenever a degenerate singular point for vorticity appears on the boundary. In recent times, investigations from the topological point of view by considering a Taylor expansion of the velocity field were also carried out for incompressible fluid near a non-simple degenerate critical point close to a stationary wall (see Gurcan, Deliceoglu & Bakker 2005).

In the present work, we make an in-depth analysis of these two phenomena by computing the flow for a large range of Reynolds numbers $500 \leqslant Re \leqslant 10\,000$ in the early stages of the flow and also computing the flow up to the post vortex shedding period for $Re = 1000$ and 5000. We show the complete evolution of the

flow for $Re = 5000$ and in the process, show the existence of two new tertiary vortex phenomena, which we term the sub-α- and sub-β-phenomena, and which have not been reported earlier. The newly developed theory of bifurcation depending on the topological structure of a two-dimensional non-divergent vector field has been applied to accurately predict recirculation areas and their time of inception as well as generation of vorticity. We also report the existence of a β-like phenomenon for $800 \leqslant Re \leqslant 3000$, which has frequently been mistaken for the β-phenomenon. To emphasize our findings we invoke the unsteady separation mechanism along the surface of the cylinder that explains the formation of a recirculation region followed by a narrow eruption of near-wall fluid.

This paper is organized in the following way. In § 2, we provide an outline of the governing equations and the discretization procedure. The validation of the code is discussed in § 3. Section 4 contains detailed discussions on the flow and the new vortex phenomena. Section 5 deals with the discussion on the formation of primary, secondary and tertiary vortices based on the boundary layer separation theory and the viscous–inviscid interaction studies. Finally, in § 6, we offer a few concluding remarks.

2. Computational formulation and methods

Here, unsteady two-dimensional Navier–Stokes equations are solved using the biharmonic pure streamfunction (Kalita & Sen 2012*a*,*b*) formulation. The formulation and auxiliary conditions are presented next.

2.1. *The governing equation and formulation*

The unsteady two-dimensional incompressible viscous flows are governed by the N–S equations. In a Cartesian (x, y) coordinate system, the non-dimensional primitive variable form of these equations for the problem of flow past a circular cylinder having unit radius, along with the equation of continuity can be written as:

$$\frac{1}{2}\frac{\partial \boldsymbol{V}}{\partial t} + (\boldsymbol{V}\cdot\boldsymbol{\nabla})\boldsymbol{V} = -\boldsymbol{\nabla} p + \frac{2}{Re}\Delta \boldsymbol{V}, \tag{2.1}$$

$$\boldsymbol{\nabla}\cdot\boldsymbol{V} = 0. \tag{2.2}$$

Here $\boldsymbol{V} = (u, v)$ is the non-dimensional velocity vector and p is the pressure. The Reynolds number Re is defined as $Re = DU_\infty/\nu$ where $D = 2a$ is the diameter of the cylinder, U_∞ is the free-stream velocity and ν kinematic viscosity. The non-dimensionalization has been carried out following Bouard & Coutanceau (1980). Introducing vorticity $\omega = \boldsymbol{\nabla}\times\boldsymbol{V} = -\partial_y u + \partial_x v$ and applying the curl operator $\boldsymbol{\nabla}\times$ to the momentum equation (2.1) we get

$$\frac{1}{2}\frac{\partial \omega}{\partial t} + (\boldsymbol{V}\cdot\boldsymbol{\nabla})\omega = \frac{2}{Re}\Delta\omega. \tag{2.3}$$

Using streamfunction ψ, which can be obtained from (2.2), we get

$$\omega = -\Delta\psi, \tag{2.4}$$

along with $(u, v) = \boldsymbol{\nabla}^\perp\psi = (\psi_y, -\psi_x)$. Equations (2.3) and (2.4) are together known as the streamfunction–vorticity form of the N–S equations. Traditionally, the primitive variable and streamfunction–vorticity formulations of the N–S equations have been the most popular approaches for computing viscous incompressible fluid flows. For flows in two dimensions, the streamfunction–vorticity formulation is more popular for its computational economy; it requires handling of only two unknowns as opposed to

three in the case of primitive variables. Furthermore, it ensures exact satisfaction of the mass conservation equation. However, the main difficulty lies with the vorticity boundary conditions which are artificial in nature. A better approach could be to use the fourth-order biharmonic streamfunction formulation of the N–S equations. This can be achieved by eliminating ω from (2.3) and (2.4) and is given as

$$\frac{1}{2}\frac{\partial}{\partial t}(\Delta\psi) + [(\nabla^{\perp}\psi)\cdot\nabla]\Delta\psi = \frac{2}{Re}\Delta^2\psi. \tag{2.5}$$

This formulation for the time-dependent N–S system in rectangular planar domains has existed (Goodrich & Sox 1989) for almost two decades. However the application of compact schemes to this formulation started with the pioneering work of Kupferman (2001), but a close look at the literature (Kupferman 2001; Ben-Artzi *et al.* 2005; Gupta & Kalita 2005; Ben-Artzi, Croisille & Fishelov 2006; Kalita & Gupta 2010) suggests that computations of flows using the biharmonic formulation has been restricted to only rectangular domains. Recently Kalita & Sen (2012*a*,*b*) have extended this scheme to domains beyond rectangular. Note that many challenging and interesting physical problems involve viscous, incompressible fluid flow in geometrically complex regions. Curvilinear coordinate systems generated to maintain coordinate lines coincident with the boundaries provide the key to the development of finite difference solutions of PDEs on regions with arbitrarily shaped boundaries.

We assume that the physical (x, y) plane can be transformed into a computational (ξ, η) plane by a conformal transformation of the form $z = z(\theta), z = x + \mathrm{i}y$ and $\theta = \xi + \mathrm{i}\eta$ $(\mathrm{i} = \sqrt{-1})$, then equation (2.5) in the computational plane reduces to

$$\begin{aligned}\frac{\partial}{\partial t}\Delta\psi = {} & a(\xi,\eta)\Delta^2\psi + b(\xi,\eta,\psi_\xi,\psi_\eta)\Delta\psi_\xi + c(\xi,\eta,\psi_\xi,\psi_\eta)\Delta\psi_\eta \\ & + d(\xi,\eta,\psi_\xi,\psi_\eta)\Delta\psi\end{aligned} \tag{2.6}$$

where

$$a(\xi,\eta) = \frac{4}{ReJ}, \quad b(\xi,\eta,\psi_\xi,\psi_\eta) = \frac{2}{J}\left(-\frac{4C}{Re} - \psi_\eta\right), \tag{2.7}$$

$$\left.\begin{aligned} c(\xi,\eta,\psi_\xi,\psi_\eta) &= \frac{2}{J}\left(-\frac{4D}{Re} + \psi_\xi\right), \\ d(\xi,\eta,\psi_\xi,\psi_\eta) &= \frac{2}{J}\left(\frac{2E}{Re} + C\psi_\eta - D\psi_\xi\right), \end{aligned}\right\} \tag{2.8}$$

$$C = \frac{J_\xi}{J}, \quad D = \frac{J_\eta}{J}, \quad E = 2C^2 + 2D^2 - \frac{J_{\eta\eta}}{J} - \frac{J_{\xi\xi}}{J}, \tag{2.9}$$

J being the Jacobian of the transformation. The components of velocity in the transformed plane are

$$u = \frac{1}{J}(\psi_\eta x_\xi - \psi_\xi x_\eta), \quad v = \frac{1}{J}(-\psi_\xi y_\eta + \psi_\eta y_\xi). \tag{2.10}$$

The benefit of using (2.5) is threefold: (i) difficulties associated with primitive variables arising mainly because of pressure are avoided; (ii) use of artificial vorticity boundary conditions is avoided and (iii) iterations involve only a single variable (ψ).

Whenever vorticity ω needs to be computed, it can be post-processed by solving the Poisson equation in the transformed plane given by

$$\Delta\psi = -J\omega. \tag{2.11}$$

2.2. *Discretization procedures*

It is well known that compact schemes provide much higher resolution than explicit higher-order upwind schemes, thus enabling one to obtain numerical solutions with significantly enhanced accuracy. Such an approach will have two major advantages: (i) the coefficient matrix resulting from the system of linear equations after discretization will have a smaller bandwidth; and (ii) no modification will be needed at grid points near the boundaries, thus facilitating easier and at times exact implementation and satisfaction of the boundary conditions. We use the following discretizations for space derivatives $\Delta^2\psi$ and $\Delta\psi$:

$$\Delta_h^2\psi_{i,j} = \delta_\xi^4\psi_{i,j} + 2\delta_\xi^2\delta_\eta^2\psi_{i,j} + \delta_\eta^4\psi_{i,j} + O(h^2), \tag{2.12}$$

$$\Delta_h\psi_{i,j} = \delta_\xi^2\psi_{i,j} + \delta_\eta^2\psi_{i,j} + O(h^2). \tag{2.13}$$

Here δ_ξ^4 denotes the Stephenson finite difference operator (Stephenson 1984) defined as

$$\delta_\xi^4\psi_{i,j} \equiv \frac{12}{h^2}(\delta_\xi\psi_{\xi_{i,j}} - \delta_\xi^2\psi_{i,j}), \tag{2.14}$$

δ_ξ^2 and δ_ξ being the usual second-order central difference operators. Compatible Padé approximations for ψ_ξ and ψ_η may be chosen as:

$$\psi_{\xi_{i,j}} = \left(\delta_\xi\psi_{i,j} - \frac{h^2}{6}\delta_\xi^2\psi_{\xi_{i,j}}\right) + O(h^4), \quad \psi_{\eta_{i,j}} = \left(\delta_\eta\psi_{i,j} - \frac{h^2}{6}\delta_\eta^2\psi_{\xi_{i,j}}\right) + O(h^4). \tag{2.15}$$

Having obtained second-order approximations for space derivatives of (2.6), our next step is to discretize time derivative and obtain a stable numerical scheme. We introduce the weighted time-average parameter λ such that $t_\lambda = (1-\lambda)t_\lambda^{(n)} + \lambda t_\lambda^{(n+1)}$ for $0 \leqslant \lambda \leqslant 1$, and approximate (2.6) as:

$$\begin{aligned}\Delta_h\psi_{i,j}^{(n+1)} = \Delta_h\psi_{i,j}^{(n)} &+ \delta t(1-\lambda)[a_{i,j}\Delta_h^2\psi_{i,j}^{(n)} + b_{i,j}\Delta_h\psi_{\xi_{i,j}}^{(n)} + c_{i,j}\Delta_h\psi_{\eta_{i,j}}^{(n)} \\ &+ d_{i,j}\Delta_h\psi_{i,j}^{(n)}] + \delta t\lambda[a_{i,j}\Delta_h^2\psi_{i,j}^{(n+1)} \\ &+ b_{i,j}\Delta_h\psi_{\xi_{i,j}}^{(n+1)} + c_{i,j}\Delta_h\psi_{\eta_{i,j}}^{(n+1)} + d_{i,j}\Delta_h\psi_{i,j}^{(n+1)}].\end{aligned} \tag{2.16}$$

Varying λ provides a class of integrators, for example forward Euler for $\lambda = 0$, backward Euler for $\lambda = 1$ and Crank–Nicolson for $\lambda = 1/2$. Using the last option, we obtain an $O(h^2; \delta t^2)$ accurate scheme for (2.6).

2.3. *Solution of algebraic systems of equations*

We now discuss the solution of algebraic systems associated with the finite difference approximation (2.16). Introducing the notation

$$\Psi = (\psi_{1,1}, \psi_{1,2}, \ldots, \psi_{m,n})^{\mathrm{T}}, \tag{2.17}$$

the resulting system of equations for $\lambda = 1/2$ in matrix form is

$$M_1\Psi^{(n+1)} = F_1(\Psi^{(n)}, \Psi_\xi^{(n)}, \Psi_\eta^{(n)}, \Psi_\xi^{(n+1)}, \Psi_\eta^{(n+1)}). \tag{2.18}$$

For a grid of size $m \times n$, the matrix M_1 has dimension mn. Due to the compact nature of our scheme M_1 is a banded matrix with nine non-zero diagonals. Also $\Psi^{(n)}$, $\Psi_\xi^{(n)}$, $\Psi_\eta^{(n)}$, $\Psi^{(n+1)}$, $\Psi_\xi^{(n+1)}$, $\Psi_\eta^{(n+1)}$ are all mn component vectors. At any time step, once $\Psi^{(n)}$ has been approximated, $\Psi_\xi^{(n)}$ and $\Psi_\eta^{(n)}$ can be obtained by solving the tridiagonal systems

$$M_2\Psi_\xi^{(n)} = F_2(\Psi^{(n)}), \quad M_3\Psi_\eta^{(n)} = F_3(\Psi^{(n)}) \tag{2.19}$$

respectively. Equations (2.19) are the corresponding matrix forms of relations (2.15). Thus the main objective now is to solve (2.18), thereby evaluating unknown vector $\Psi^{(n+1)}$. But a difficulty arises due to the presence of the $(n+1)$th time level gradients of Ψ on the right-hand side of (2.18) as those quantities will be available only after solving for the streamfunction at the $(n+1)$th time level. To overcome this difficulty we adopt a predictor–corrector approach. By setting $\lambda = 0$ in (2.16) we get a first-order time-accurate formula which has the matrix representation

$$M_4\Psi_{old}^{(n+1)} = F_4(\Psi^{(n)}, \Psi_\xi^{(n)}, \Psi_\eta^{(n)}). \tag{2.20}$$

Here M_4 is a matrix with only five non-zero diagonals and we have the advantage that $\Psi^{(n+1)}$ can be estimated directly. Thus we have the following algorithm:

(i) predict $\Psi_{old}^{(n+1)}$ using (2.20);
(ii) predict $\Psi_{\xi_{old}}^{(n+1)}$, $\Psi_{\eta_{old}}^{(n+1)}$ using (2.19);
(iii) correct $\Psi_{new}^{(n+1)}$ using (2.18);
(iv) correct $\Psi_{\xi_{new}}^{(n+1)}$, $\Psi_{\eta_{new}}^{(n+1)}$ using (2.19);
(v) if $\|\Psi_{new}^{(n+1)} - \Psi_{old}^{(n+1)}\| < \epsilon$ then $\Psi^{(n+1)} = \Psi_{new}^{(n+1)}$;
(vi) $\Psi_{old}^{(n+1)} = \Psi_{new}^{(n+1)}$, goto step (iii).

As the direct solution of any of the above linear system is impractical all the computations were performed using the biconjugate gradient stabilized (BiCGStab) method where, thanks to the compact grid, it is easy to implement matrix vector multiplication $M_1\Psi$ without the need of storing all the entries of the matrix M_1. The convergence criterion for BiCGStab iteration based on the norm of the residual was set at 10^{-8} and the stopping criterion for the corrector was set at 10^{-12}.

2.4. *Description of the problem and corresponding initial and boundary conditions*

We assume the cylinder to be of unit radius placed in an infinite domain. A uniform grid spacing is employed along the cross-radial θ-direction and non-uniform grid spacing in the radial r-direction with clustering around the surface of the cylinder using the transformation $x = e^{(\pi\xi)}\cos(\pi\eta)$, $y = e^{(\pi\xi)}\sin(\pi\eta)$. The domain over which the solution of (2.6) is obtained is an annular one with inner radius unity and outer radius R_∞. We non-dimensionalize the flow variables by taking $x = x^*/a$, $y = y^*/a$, $u = u^*/U_\infty$, $v = v^*/U_\infty$, $t = t^*U_\infty/D$, $Re = DU_\infty/\nu$; u^*, v^* are the dimensional velocities along the x^*-, y^*- directions respectively and ν is the kinematic viscosity. $D = 2a$ is the diameter of the cylinder. The biharmonic equation (2.6) then reduces to

$$Re\frac{\pi^2 e^{2\pi\xi}}{4}\frac{\partial}{\partial t}\Delta\psi = \Delta^2\psi - \left(4\pi + \frac{Re}{2}\psi_\eta\right)\Delta\psi_\xi + \frac{Re}{2}\psi_\xi\Delta\psi_\eta + 2\pi\left(2\pi + \frac{Re}{2}\psi_\eta\right)\Delta\psi. \tag{2.21}$$

The corresponding finite difference approximation with $\lambda = 1/2$ is given by

$$\begin{aligned} Re\frac{\pi^2 e^{2\pi\xi_i}}{4}\Delta_h\psi_{i,j}^{(n+1)} &= Re\frac{\pi^2 e^{2\pi\xi_i}}{4}\Delta_h\psi_{i,j}^{(n)} \\ &+ \frac{\delta t}{2}\left[\Delta_h^2\psi_{i,j}^{(n)} - \left(4\pi + \frac{Re}{2}\psi_{\eta_{i,j}}^{(n)}\right)\Delta_h\psi_{\xi_{i,j}}^{(n)}\right. \\ &\left. + \frac{Re}{2}\psi_{\xi_{i,j}}^{(n)}\Delta_h\psi_{\xi_{i,j}}^{(n)} + 2\pi\left(2\pi + \frac{Re}{2}\psi_{\eta_{i,j}}^{(n)}\right)\Delta_h\psi_{i,j}^{(n)}\right] \\ &+ \frac{\delta t}{2}\left[\Delta_h^2\psi_{i,j}^{(n+1)} - \left(4\pi + \frac{Re}{2}\psi_{\eta_{i,j}}^{(n+1)}\right)\Delta_h\psi_{\xi_{i,j}}^{(n+1)}\right. \\ &\left. + \frac{Re}{2}\psi_{\xi_{i,j}}^{(n+1)}\Delta_h\psi_{\xi_{i,j}}^{(n+1)} + 2\pi\left(2\pi + \frac{Re}{2}\psi_{\eta_{i,j}}^{(n+1)}\right)\Delta_h\psi_{i,j}^{(n+1)}\right]. \quad (2.22) \end{aligned}$$

This is the discretized equation we intend to use for numerical simulation.

We estimate the boundary conditions for the streamfunction and its first-order derivatives as follows.

(*a*) On the surface of the cylinder $\xi = 0$, $u = v = 0 \Rightarrow \psi_\xi = 0$, $\psi_\eta = 0$, $\psi = 0$.

(*b*) Far upstream $u = U_\infty$, $v = 0 \Rightarrow \psi_\xi = \pi e^{(\pi\xi)}\sin(\pi\eta)$, $\psi_\eta = \pi e^{(\pi\xi)}\cos(\pi\eta)$ and $\psi = e^{(\pi\xi)}\sin(\pi\eta)$ which corresponds to the potential flow.

(*c*) Far downstream we use the Neumann condition that $\partial V_r/\partial\xi = 0 = \partial V_t/\partial\xi$. The one-sided second-order approximation translates these conditions to, $\psi_{\eta_{imax,j}} \doteq (4e^{\pi h}\psi_{\eta_{imax-1,j}} - e^{2\pi h}\psi_{\eta_{imax-2,j}})/3$, $\psi_{\xi_{imax,j}} \doteq (4e^{\pi h}\psi_{\xi_{imax-1,j}} - e^{2\pi h}\psi_{\xi_{imax-2,j}})/3$ respectively.

It should be noted here that once the vortex shedding starts, one needs to use convective boundary condition $\partial\psi/\partial t + U_\infty\partial\psi/\partial x = 0$ for ψ in the downstream. When asymmetry is about to set in the flow, the potential boundary condition downstream of the flow for ψ was replaced by a convective boundary condition and was found to be quite efficient. Moreover, for flows with higher Re, the convective boundary condition at the very initial stage of flow does not work well. Thus if one wishes to simulate a flow from very beginning to the final vortex shedding stage, an ideal choice will be to march the first few iterations (say) till non-dimensional time $t = 0.25$ with the potential boundary condition and then to proceed with the convective boundary condition. As far as the initial condition is concerned we have started with $\psi = 0$ everywhere except at the boundary as also $\psi_\xi = \psi_\eta = 0$ everywhere except at the upstream boundary.

The drag $\mathfrak{D}$ on the surface of a cylinder of radius r in a fluid of density ρ is $\mathfrak{D} = \rho r U_\infty^2 C_D$, where C_D is the non-dimensional drag coefficient. In terms of a pure streamfunction the formula for C_D (Kalita & Sen 2012*a*,*b*) can be written as

$$C_D = \frac{2}{Re\pi^2}\int_0^2 (3\pi\psi_{\xi\xi} - \psi_{\xi\xi\xi})\sin(\pi\eta)\,d\eta. \quad (2.23)$$

Similarly the lift coefficient is $C_L = (2/Re\pi^2)\int_0^2(3\pi\psi_{\xi\xi} - \psi_{\xi\xi\xi})\cos(\pi\eta)\,d\eta$. Following Chang & Chern (1991) the surface pressure P at each point on the surface of the cylinder can be obtained by integrating the momentum equation (2.1) radially from infinity to the cylinder surface. Prescribing the value of pressure to be zero at infinity, finally in the transformed (ξ, η) plane it can be expressed exclusively in terms of the

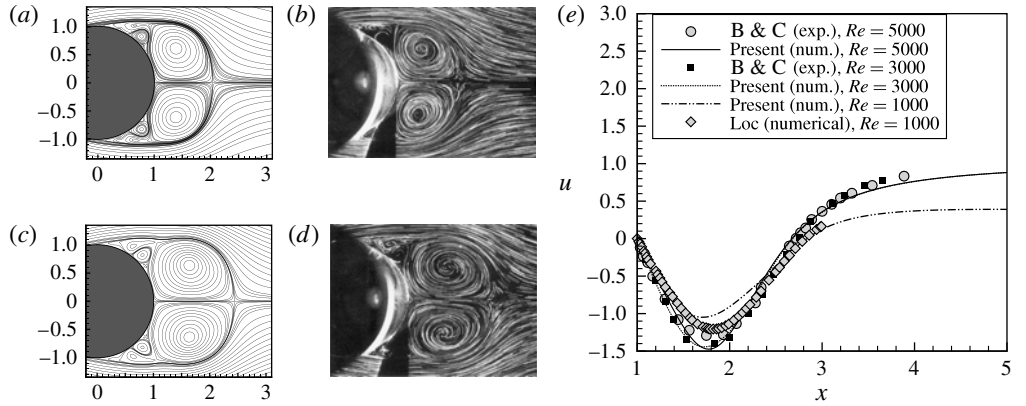

FIGURE 2. Comparison of streamlines with experimental results of Bouard & Coutanceau (1980)(C & B) for $Re = 5000$: (*a*) present ($t = 2.0$), (*b*) experimental ($t = 2.0$), (*c*) present ($t = 2.5$) and (*d*) experimental ($t = 2.5$); and (*e*) comparison of velocity distribution on the flow axis between experimental (Bouard & Coutanceau 1980), numerical (Loc 1980) and the present results at $t = 3.0$ for $Re = 1000$, 3000 and 5000.

streamfunction as

$$P(\eta) = \int_0^\infty \left(-\frac{2}{ReJ}(\psi_{\xi\xi\eta} + \psi_{\eta\eta\eta}) + \frac{1}{2}\frac{\partial \psi_\eta}{\partial t} - \frac{\psi_\xi}{J}(\psi_{\xi\xi} + \psi_{\eta\eta}) \right) \mathrm{d}\xi + \frac{1}{2}. \quad (2.24)$$

All the above integrals have been evaluated by using Simpson's one-third formula.

Also, the expressions for pressure gradients on the surface of the cylinder can be obtained from momentum equation (2.1). In terms of the pure streamfunction they are

$$p_r = \frac{2}{Re}\frac{\psi_{\xi\xi\eta}}{\pi^3} \quad \text{and} \quad p_\theta = \frac{2}{Re}\left(\frac{-\psi_{\xi\xi\xi} + 2\pi\psi_{\xi\xi}}{\pi^3} \right), \quad (2.25)$$

subscripts r and θ denoting derivatives along the radial and cross-radial directions respectively.

3. Validation of the code

3.1. *Comparison with earlier results*

The finite difference scheme described in the previous section is validated by comparing our numerical results with available experimental and numerical results. First, in figure 2(*a–d*), our computed streamlines for $Re = 5000$ at $t = 2.0$ and $t = 2.5$ are compared with the experimental visualization of Bouard & Coutanceau (1980). Our numerical simulation is an excellent match with the experiments and is much closer to the experiments than the numerical simulations of Sengupta & Sengupta (1994) and Sanyasiraju & Manjula (2005) obtained through compact schemes. As mentioned in the introduction, not many quantitative numerical results are available for $Re = 5000$. The only quantitative experimental result available is the velocity distribution on the flow axis at time $t = 3.0$ provided by Bouard & Coutanceau (1980); we compare this with our numerical results in figure 2(*e*) and once again they are an excellent match. As our narrative will also include some description of the flow for $Re = 1000$ and 3000, we have included the comparison of our numerical results for $Re = 3000$ with the experimental results of Bouard & Coutanceau (1980) and

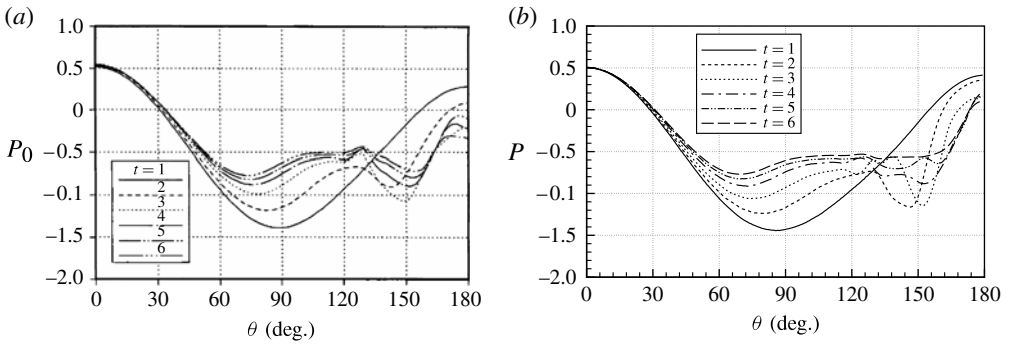

FIGURE 3. Pressure distribution on the surface of the cylinder for $Re = 3000$ at different times: (*a*) Chang & Chern (1991) and (*b*) present.

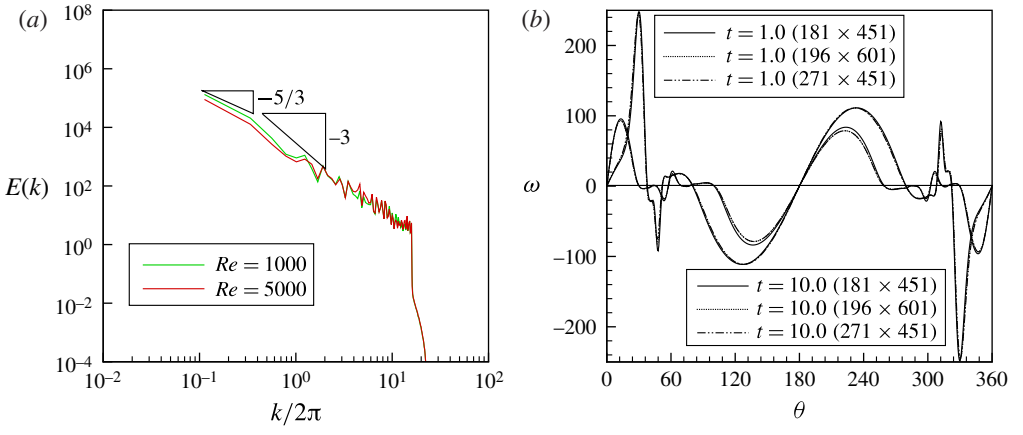

FIGURE 4. Code robustness and grid independence study: (*a*) energy spectra for the flow at two Re and (*b*) surface vorticity distribution on three different grids.

the numerical results of Loc (1980) for $Re = 1000$ for the same instant of time in figure 2(*e*). The slight disparity between Loc's (1980) result and ours could be from the fact that he used a very coarse grid (81×41) for his computation compared to ours (271×451).

Further, we compare our computed pressure distribution on the surface of the cylinder for $Re = 3000$ at different times with those of Chang & Chern (1991) in figure 3. Note that the θ range in figure 3(*b*) is reversed in order to match with Chang & Chern (1991) where θ is defined in a direction opposite to the one used by us. Once again, a very close resemblance can be seen between these figures.

In order to test the robustness of our code, we also compute the energy spectra for $Re = 1000$ and 5000 for the fully developed flow and present them in figure 4(*a*). Note that in two dimensions the inverse cascade drives energy from small to spatially smooth and large eddies. The phenomenon involves an interplay between small and large scales. For both the Re values considered here, a very close resemblance between the graph of k^{-3} versus k and that of $E(k)$ versus k can be seen. Also indicated in

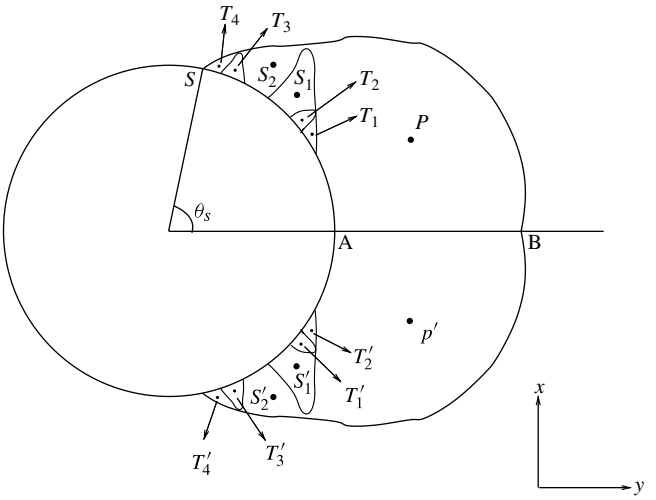

FIGURE 5. Schematic diagram of the vortex structures. The letters P, S and T denote primary, secondary and tertiary vortices respectively.

the figure is the $k^{-5/3}$ variation below the energy injection wavenumber. Both these observations are in conformity with the existing theory (Singh & Mittal 2004).

3.2. *Outer boundary location and mesh convergence*

In order to study the influence of grid size and the location of the outer boundary on the characteristics of the flow, computations are carried out on five meshes of sizes 181×451 with $R_\infty \approxeq 12$, 196×601 with $R_\infty \approxeq 8$, 271×451 with $R_\infty \approxeq 43$, 261×801 with $R_\infty \approxeq 8$ and 301×1201 with $R_\infty \approxeq 5$. The time step for the first three meshes is 5×10^{-4}, and 1.0×10^{-4} for the remaining two. Except for the third grid, R_∞ is kept small as we are interested in the flow only in the vicinity of the surface of the cylinder at the earlier stages of the flow; the third grid is specifically chosen for examining the flow in the post vortex shedding period. In table 1, we show the separation angle θ_S, the wake length L and the location of the centre of the upper primary vortex $(\bar{x}, \bar{y})$ at different times computed on these five grids. The maximum differences (which are computed for all the times presented in the table, taken two grids at a time) in θ_S, L and $\bar{x}$ values are below 5 % in all the cases. However, for a better resolution of the flow, the results presented in the subsequent sections correspond to mesh M_5 for $t \leqslant 10$ and M_4 beyond that except when the time history of the drag and lift coefficients is discussed in the post shedding period, when we use M_3. In figure 4(*b*) we present the surface vorticity distribution at times $t = 1.0$ and $t = 10.0$ on the first three grids; once again one can see that they are extremely close to each other.

4. Observations and new vortex phenomena

First we shall provide a detailed description of the interplay between the primary and secondary vortices leading to the so-called α- and β-phenomena. Next, we will examine the hitherto unreported interplay amongst the primary, secondary and tertiary vortices. Finally, we shall reflect upon some distinct features of the β-phenomenon that have escaped the attention of the earlier studies. Readers can refer to figure 5 for a schematic diagram of the vortex structures where the letters P, S and T denote primary,

https://doi.org/10.1017/jfm.2013.272 Published online by Cambridge University Press

Mesh		M_1	M_2	M_3	M_4	M_5
Grid size		181 × 451	196 × 601	271 × 451	261 × 801	301 × 1201
R_∞		12	8	43	8	5
$t = 1$	θ_S	80.38	80.20	80.38	77.84	78.74
	L	0.216	0.212	0.207	0.217	0.231
	$(\bar{x}, \bar{y})$	(0.9484, 0.6498)	(0.9408, 0.6540)	(0.9378, 0.6373)	(0.9351, 0.6570)	(0.9374, 0.6589)
$t = 2$	θ_S	91.66	91.12	92.21	89.79	89.47
	L	0.979	0.983	0.978	0.981	1.037
	$(\bar{x}, \bar{y})$	(1.3505, 0.6026)	(1.3599, 0.6055)	(1.3592, 0.5881)	(1.3599, 0.6138)	(1.3920, 0.6112)
$t = 3$	θ_S	94.75	94.76	95.48	93.22	92.65
	L	1.672	1.694	1.668	1.690	1.757
	$(\bar{x}, \bar{y})$	(1.7539, 0.5834)	(1.7886, 0.5606)	(1.7548, 0.5702)	(1.8012, 0.5698)	(1.7666, 0.5335)
$t = 4$	θ_S	96.39	96.03	97.23	94.98	94.41
	L	2.082	2.099	2.094	2.098	2.177
	$(\bar{x}, \bar{y})$	(1.7950, 0.6251)	(1.8076, 0.6295)	(1.7734, 0.6072)	(1.8070, 0.6359)	(1.7765, 0.5979)
$t = 5$	θ_S	97.30	97.30	98.08	95.88	94.94
	L	2.411	2.446	2.419	2.443	2.514
	$(\bar{x}, \bar{y})$	(1.9488, 0.7716)	(1.9556, 0.7742)	(1.9454, 0.7702)	(1.9454, 0.7701)	(2.0177, 0.7728)

TABLE 1. Effect of the mesh size and the outer radius location on the characteristics of the flow (the separation angle θ_S, the wake length L and the location of the centre of the upper primary vortex $(\bar{x}, \bar{y})$, for $Re = 5000$ at five different times.

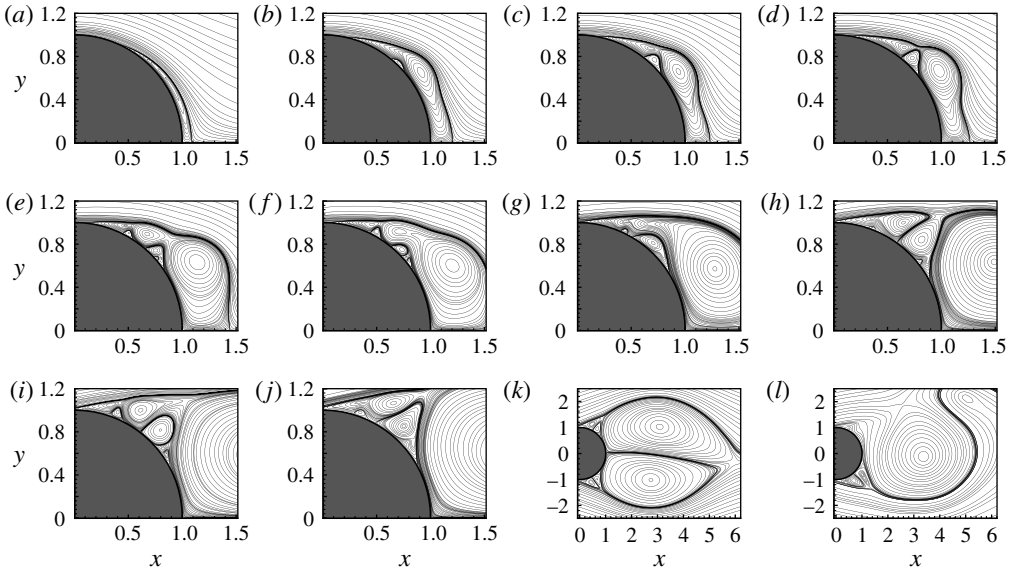

FIGURE 6. Evolution of streamlines for $Re = 5000$ for flow past a circular cylinder at: (*a*) $t = 0.5$, (*b*) 0.9, (*c*) 1.0, (*d*) 1.1, (*e*) 1.35, (*f*) 1.45, (*g*) 1.7, (*h*) 2.25, (*i*) 2.9, (*j*) 4.0, (*k*) 20.0 and (*l*) 24.5.

secondary and tertiary vortices respectively: the primed letters denote vortices on the lower half of the cylinder while non-primed ones refer to vortices on the upper half. A better understanding of the location of these vortices is provided by the vorticity distribution curve in figure 14 in § 4.4 where several zones have been marked over the surface of the cylinder.

4.1. *Primary and secondary vortex phenomena*

Figure 6(*a–l*) depicts the evolution of primary and secondary vortices for $Re = 5000$ and the occurrence of α- and β-phenomena in the process. At time approximately $t = 0.25$, a pair of symmetric vortices is clearly visible behind the cylinder. With time, this pair of vortices grows symmetrically in size where one is the mirror image of the other with respect to x-axis. The core of the primary vortex lying above the x-axis (denoted by P in figure 5) gathers strength as time progresses and moves downstream in an upward direction (figure 6*a,b*). Note that unless otherwise stated the description of the flow will pertain to only on the top half of the cylinder as the flow maintains its symmetry till a certain time. Meanwhile, at around time $t = 0.85$, the secondary phenomenon starts with the second separation on the surface of the cylinder as can be seen in figure 6(*b*). This separation leads to the formation of a secondary vortex (S_1 in figure 5) that starts growing in size (see figure 6*b–d*) which can also be seen from the three alternately rotating zones of vorticity on the surface of the cylinder in figure 14(*a*). At around $t = 1.0$ this secondary vortex becomes prominent (figure 6*c*), dividing the primary vortex into two chambers, one of which is the core. Nevertheless the weaker part (S_2 in figure 5; we shall also refer to it as the arm of the primary vortex) maintains some communication with its core part. For some time both the core and the secondary vortex acquire strength (see figure 6*c,d*) and the channel of communication between the two parts of the primary vortex becomes narrow at

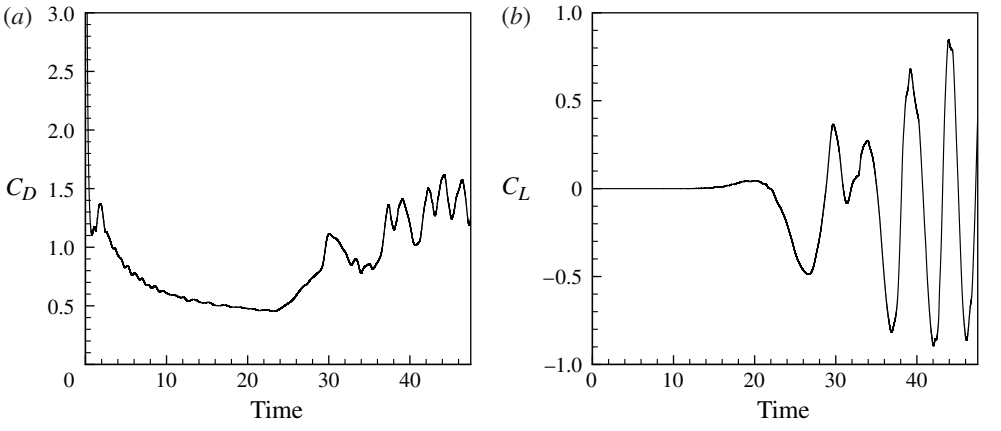

FIGURE 7. Time history of (*a*) drag and (*b*) lift coefficients of the flow past circular cylinder for $Re = 5000$.

time $t \approxeq 1.1$ (figure 6*d*). But as the primary vortex becomes bigger in size again, both its parts (namely P and S_2) start getting stronger and engulf the secondary vortex S_1 from left and right, reducing its strength and size at time $t \approxeq 1.35$ (figure 6*e*). This is what Bouard & Coutanceau (1980) described as the β-phenomenon.

A very short time thereafter, the arm S_2 of the primary vortex gets reduced in size and strength ($t = 1.45$, figure 6*f*) and is re-aligned to the main primary vortex to form one main vortex again ($t = 1.7$, figure 6*g*). Then, the secondary vortex S_1 grows in strength again and splits the main primary vortex again to recreate the arm. The arm S_2 grows in size and strength side by side with the other secondary vortex S_1 (figure 6*h,i*) and eventually they are almost equal in size and strength ($t = 2.5$, figure 2(*c,d*). They constitute what Bouard & Coutanceau (1980) described as 'a pair of secondary vortices' and which is the α-phenomenon. Both these secondary vortices $\boldsymbol{S}_1$ and $\boldsymbol{S}_2$ continue to grow in size and strength (figure 6*i,j*).

During the time considered above, the main primary vortices also grow in size and strength more rapidly than the secondary ones and their centres shift downstream (figures 6*k* and 8*b*). The upper and lower primary vortices lose their symmetry about the x-axis at the tail of the wake even though the formations just behind the cylinder still maintain their symmetry till $t = 20.0$ (figure 6*k*) including the pair of secondary vortices responsible for the α-phenomenon. In the meantime the upper and lower primary vortices alternately exceed each other in size and strength while the free stream keeps on slowly sweeping their centres downstream. The lower primary vortex, while growing in size, pushes the upper primary vortex upwards and breaks it into two parts for a very short time. When the upper primary vortex becomes completely detached from the surface of the cylinder and is no longer available to cushion the vortices S_1 and S_2, the free stream finally sweeps these secondary vortices away. This is when no trace of the so-called α-phenomenon can be seen at the top half of the surface of the circular cylinder for the first time after its inception (figure 6*l*). The breaking in symmetry in the flow which eventually leads to the shedding of vortices can also be seen from figure 7 where the time histories of drag (C_D) and lift (C_L) coefficients are shown till $t = 47.5$; once shedding is activated, the mean value of C_D is observed to be 1.41.

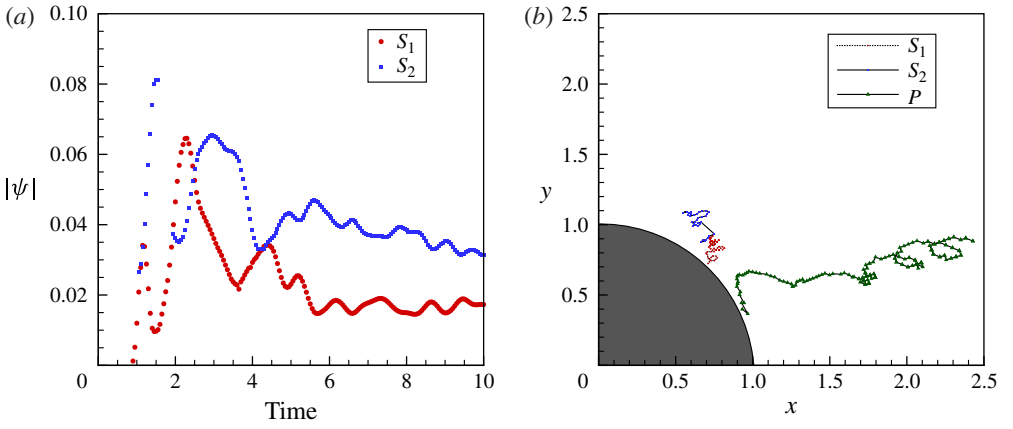

FIGURE 8. For $0 < t \leqslant 10$, $Re = 5000$: (a) the $|\psi|$ values at the centres of S_1 and S_2 and (b) the motion of the centres of S_1, S_2 and P.

Meanwhile, at the bottom half of the cylinder, the 'pair of secondary vortices', because of the cushion still provided by the lower primary vortex, continues to exist. At the same time the secondary vortices S_1' and S_2' begin to grow in size, pushing the lower primary one, and the α-phenomenon structure is broken.

It is well known that the magnitude of the streamfunction values at the centres of the vortices is a good indication of their respective strengths. We present the time history of the strengths of the secondary vortices constituting the α-phenomenon in terms of the streamfunction values at their centres in figure 8(a); note that the ψ values at the centre of S_2 are actually negative. This is probably the first time the strength of the secondary vortices constituting the α-phenomenon has been quantified. At $t = 2.5$, their strengths become almost equal to each other for the first time and then again in the vicinity of $t = 4.0$. It is interesting to note that most of the time, while the vortices S_1 and S_2 look equivalent in size, their strengths are quite different from each other as can be seen from figure 8(a). This is also true for figure 1 where streamlines are depicted for $Re = 3000$ at time $t = 2.5$ (the Re value and the instant at which Bouard & Coutanceau 1980 coined the term α-phenomenon); here S_1 and S_2, despite looking almost equal in size, have ψ values 0.0280649 and -0.0445097 respectively at their centres. A natural consequence of this observation is to redefine the α-phenomenon, which exists:

(i) in the strong sense when the secondary vortices forming the 'pair of vortices' are not only equivalent in size, but also when their strengths are almost equal to each other at least once during the evolution of the flow;

(ii) in the weak sense when the secondary vortices forming the 'pair of vortices' are only equivalent in size.

The x, y phase-planes of these secondary vortex centres along with that of the primary vortex P are shown in figure 8(b). From the figure it is clear that the centres of S_1 and S_2 remain clustered near the surface of the cylinder while one can see a gradual upward downstream movement of the centre of P.

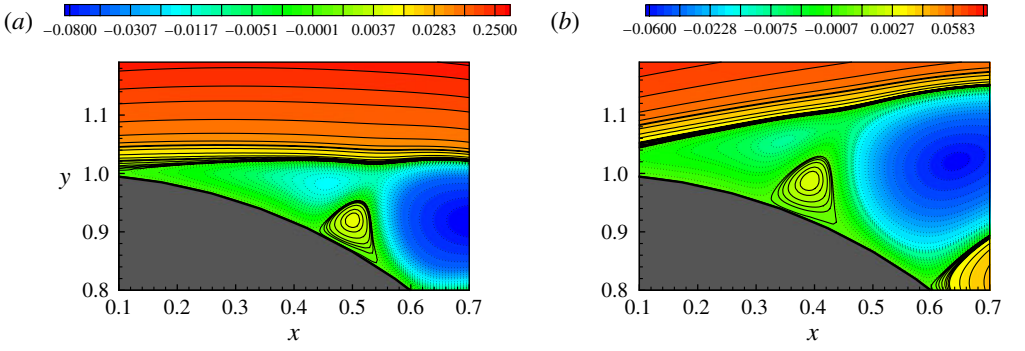

FIGURE 9. The streamlines representing sub-β-phenomenon for (*a*) $t = 1.45$ and (*b*) 3.15 for $Re = 5000$.

4.2. *Tertiary vortex dynamics*

4.2.1. *The sub-α- and sub-β-phenomenon*

Next, we provide a detailed discussion on the tertiary vortex dynamics, again for $Re = 5000$ which, to the best of our knowledge has not been reported elsewhere. From $t \approxeq 1.2$ onwards, a similar event parallel to the β-phenomenon can be observed with the formation of a tertiary vortex T_3 (see figure 5) on the surface of the cylinder cushioned by the secondary vortex S_2. A close look at figure 6(*e*) reveals that this vortex makes its appearance somewhere around $\theta = 60°$; note that during this time the centre of secondary vortex S_1 moves down to the position $\theta = 36°$ on the surface of the cylinder. This new tertiary vortex, while slowly growing in size and strength, almost replicates the role played by S_1 for the primary vortex P (see figure 6*f* at $t = 1.45$): it splits S_2, the arm of primary vortex, into two parts T_3 and T_4 (figures 5 and 9*a*), thus creating a phenomenon which we term the sub-β-phenomenon. We define this phenomenon as where a secondary vortex, part of which is bounded by the free stream, is split by the tertiary vortex cushioned by it. This sub-β-phenomenon persists till $t = 1.6$ when the secondary vortex S_2 and its arm coalesce back into one vortex. The tertiary vortex T_3 persists up to $t = 2.4$ and disappears afterwards to resurface again at $t = 2.75$. This leads to another sub-β-phenomenon which is clearly seen at $t = 3.15$ (figure 9*b*) and persists till $t = 4.0$ after which S_2 and its arm once again coalesce back to form one single vortex.

Meanwhile one can observe another event analogous to the α-phenomenon occurring at the secondary and tertiary level as early as $t \approxeq 1.25$; here one can glimpse a tertiary vortex T_2 (figures 5 and 6*e*) at the location $\theta = 43°$ which in fact was formed at $t = 1.116$ (more on this in § 5) when the strength of the secondary vortex S_1 surrounding it has a maxima with $\psi = 0.0353114$ at its centre that leads to an adverse pressure gradient. Within a short period of time, at around $t = 1.45$ this tertiary vortex grows in strength and size and splits the secondary vortex into two parts T_1 (we shall also refer to it as the arm of S_1) and T_2 (figures 5 and 10*a*) auguring a phenomenon which we term the sub-α-phenomenon. We define this phenomenon as one where two tertiary vortices form 'a pair of tertiary vortices' which are either equivalent in strength or size. At time $t = 1.65$, this tertiary vortex T_2 merges with the secondary one and the split part T_1 of the secondary vortex S_1 gets re-attached. Eventually the parts of this secondary vortex coalesce back into one vortex (figure 6*g*). This phenomenon is seen again at time $t = 2.545, 3.715, 5.55$ and 8.0 (figure 10*b,c*);

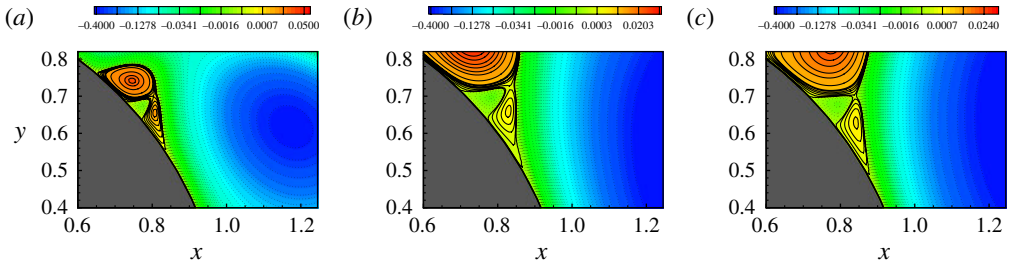

FIGURE 10. The streamlines representing sub-α-phenomenon at (*a*) $t = 1.45$, (*b*) $t = 3.715$ and (*c*) $t = 8.0$ for $Re = 5000$.

Vortex centre	$t = 1.450$	$t = 2.545$	$t = 3.715$	$t = 5.500$	$t = 8.000$	$t = 20.55$
T_1	0.00159542	0.00215581	0.00170425	0.000908059	0.000761779	0.0002712467
T_2	−0.00120229	−0.00247031	−0.0004427	−0.000910168	−0.000237116	−0.000280849

TABLE 2. Streamfunction ψ values at the centres of the tertiary vortices constituting the sub-α-phenomenon for $Re = 5000$.

these instances correspond to the times when the strengths of these tertiary vortices forming the sub-α-phenomenon are closest to one another in magnitude (see table 2). Note that till now, the appearance of these tertiary vortices was almost symmetric about the x-axis with similar occurrences at the lower half of the cylinder as well. After a long period of time, they reappear again at around $t = 20.0$, when the flow is distinctly asymmetric, this time only on the top half of the cylinder with a much reduced strength (see table 2). However, they persist for a much longer interval of time of around 2.0. Figure 10 and table 2 clearly indicate that the sub-α-phenomenon also exists both in the strong and weak sense. Note that in all the cases, the tertiary vortices T_1, T_2, T_3 and T_4 are much smaller in size and weaker in strength than their secondary counterparts S_1 and S_2. Note that in figures 9 and 10 the dotted lines correspond to negative contour values.

4.2.2. *The sub-α-phenomenon preceded by the sub-β-phenomenon*

The sub-α- and sub-β-phenomena described above occurred in isolation where neither the sub-β-phenomenon led to the sub-α-phenomenon nor was the sub-α-phenomenon preceded by the sub-β-phenomenon. We have already seen in § 4.1 that for $Re = 5000$, the α-phenomenon is preceded by the β-phenomenon. Likewise, we also found that at times the sub-α-phenomenon is preceded by the sub-β-phenomenon. However, the duration of such an occurrence is very short. We observed it for the very early stages of the flow for $Re = 8000$ in the time range $1.0 \leqslant t \leqslant 1.4$. Here, the tertiary vortex T_3 appears at around $t = 1.0$ and becomes clearly visible at $t = 1.1$ as can be seen from figure 11(*a*). It grows in size and strength and splits the secondary vortex S_2 into two parts T_3 and T_4 leading to the formation of a pair of tertiary vortices (figure 11*b*,*c*). At $t = 1.3$, the ψ values at the centres are -0.0113653 and 0.0098353. A similar sequence of events is again observed during $1.9 \leqslant t \leqslant 2.3$. The tertiaries T_3 and T_4 remain persistent approximately till $t = 4.5$. Note that the difference between

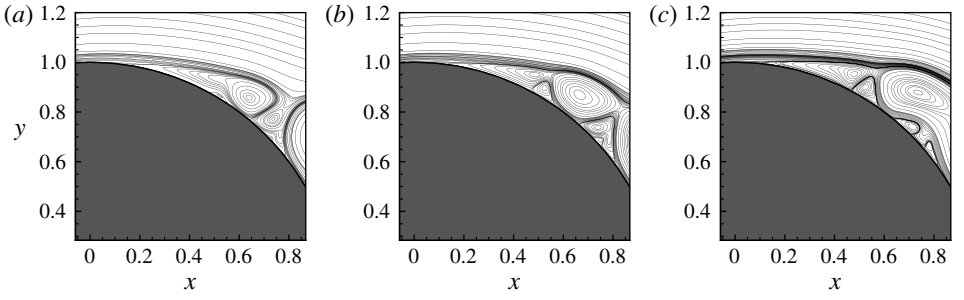

FIGURE 11. The sub-β-phenomenon followed by the sub-α-phenomenon: (*a*) $t = 1.1$, (*b*) $t = 1.2$ and (*c*) $t = 1.3$ for $Re = 8000$.

the sub-β-phenomenon described here and the one in § 4.2.1 is that the secondary vortex S_2 and its arm do not coalesce to form one single vortex again.

The occurrence of the sub-α-phenomenon preceded by the sub-β-phenomenon is also seen for $Re = 9500$ and $Re = 10\,000$ in the very early stages of the flow in the vicinity of $t = 1.0$ and then again around $t = 2.0$.

4.3. *β-like phenomenon*

Bouard & Coutanceau (1980) coined the terms α- and β-phenomena probably because of the resemblance of the vortex structures to the Greek letters α and β (figure 1). Though their description of the α-phenomenon did not have any ambiguity, the β-phenomenon deserves more in-depth examination as there is much more to it than has been described by them. For example, while portraying the β-phenomenon, they have stated that the structure of the vortex pair (constituting the β-phenomenon) is roughly similar to that for the α-phenomenon which 'however differ in details'. However, they did not discuss these details. They also report experimental evidence that the α-phenomenon is in the range of $800 \leqslant Re \leqslant 5000$ and we have already seen that the α-phenomenon is preceded by the β-phenomenon for $Re = 5000$. This may give the impression that in order for the α-phenomenon to take place, it must be preceded by the β-phenomenon. In this section, we shall show that this is not the case, which, in the process will also enable us to provide a distinct characterization of the β-phenomenon.

In figure 12, we show the events leading to the α-phenomenon for $Re = 3000$. Here at time $t = 1.5$, one can clearly see the secondary vortex splitting the main primary vortex into two parts. The arm of the main primary vortex is reduced in size gradually ($t = 1.75$) and after a while starts growing again ($t = 2.0$) leading to the formation of two secondary vortices of almost equal size and strength and hence the α-phenomenon ($t = 2.25$). Though figure 12(*a–c*) indicates a β-like phenomenon, an important component is missing here. Once split by the secondary vortex, the main primary vortex and its arm still remain detached; here the 'forewake' has not completely vanished to form a 'main wake', unlike the one described by Bouard & Coutanceau (1980) for $Re = 9500$. The same sequence of events can also be seen for $Re = 5000$ in figure 6(*f,g*).

A detailed study of the development of primary and secondary vortices depicted through the vorticity field was carried out by Koumoutsakos & Leonard (1995) for $Re = 3000$ and 9500. Analogous to the formation and subsequent development of secondary vortices for $Re = 3000$ as reported above, the authors captured the

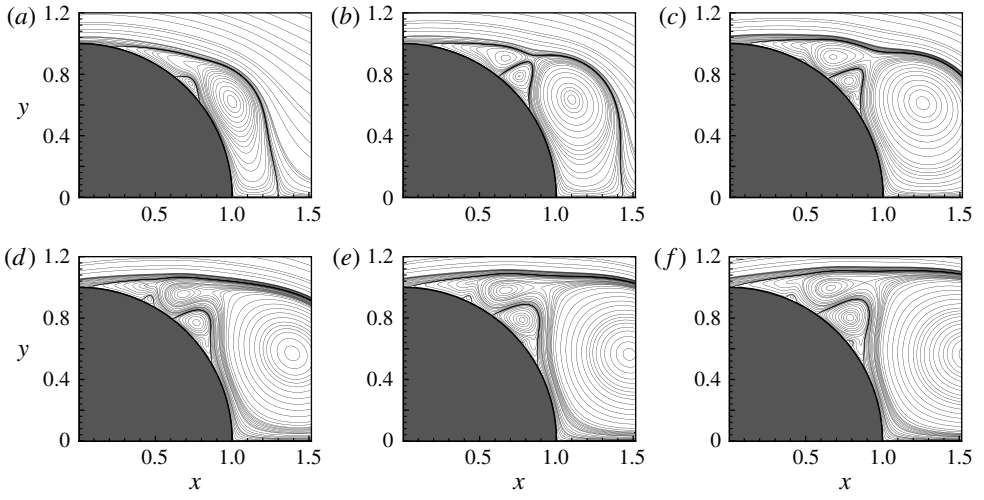

FIGURE 12. β-like phenomenon leading to the α-phenomenon for $Re = 3000$: (*a*) $t = 1.0$, (*b*) $t = 1.25$, (*c*) $t = 1.5$, (*d*) $t = 1.75$, (*e*) $t = 2.0$ and (*f*) $t = 2.25$.

generation of secondary vortices, which in turn attempt to penetrate the primary vortex field somewhere between $t = 2.0$ and 3.0. At later times they have also detailed an increase in the drag coefficient due to the increase in the strength of the primary vortex. The results depicted by us using streamline contours on a relatively coarser grid are in good agreement with the findings of Koumoutsakos & Leonard (1995) where up to a million computational elements were used.

Note that the formation of the secondary vortex S_1 which pushes the primary vortex P to split into two parts, gives rise to a bulge-like shape to the main vortex during this time (see figures 1*b*, 6*d,e*). This is however absent during the splitting of the primary vortex at the early stages for $Re = 3000$ (figure 12*b,c*). It is worth mentioning here that the sub-β-phenomenon which preceded the sub-α-phenomenon described in § 4.2.2 is more reminiscent of the β-like phenomenon than the β-phenomenon as the arm of the secondary vortex S_2 (S_2') does not get re-attached to its main vortex S_2 again.

4.4. *Multiple separation zones*

The formation of the primary, secondary and tertiary vortices gives way to multiple separation zones on the surface of the cylinder. For $Re = 5000$, as early as $t = 1.35$ (figure 13*a*), one can see the occurrence of multiple separation zones which become more distinct at $t = 2.9$ (figures 6*i* and 13*b*). Also for higher Re, for which the computation is indeed challenging and more interesting, the flow includes more tertiary recirculation zones on the surface at quite early stages as can be seen from figure 13(*c*) for $Re = 10\,000$ at $t = 2.5$. A similar portrayal of the development, roll-up and eventual detachment of the primary vortex from the body was also depicted by Koumoutsakos & Leonard (1995), but for $Re = 9500$. The effect of such a detachment on secondary vortices and its shape at time $t = 2.5$ have been discussed by the authors as well. However, for complete understanding one needs to carefully examine the vorticity distribution on the surface of the cylinder. The extent and size of these vortices can be gauged by the alternate positive and negative values of vorticity on the surface of the cylinder. Moreover, the time of birth of the secondary and tertiary vortices can be found by accurately computing the instant when the curve of surface

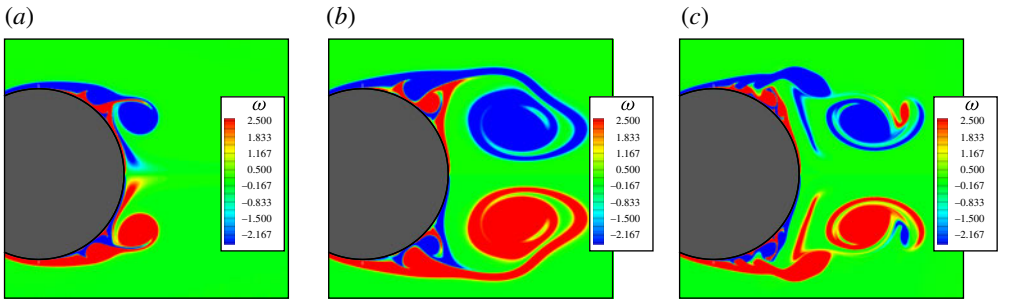

FIGURE 13. Existence of multiple separation zones on the surface of the cylinder: vorticity contours for $Re = 5000$, at (*a*) $t = 1.35$, (*b*) $t = 2.9$, and for $Re = 10\,000$ at (*c*) $t = 2.5$.

vorticity touches the $\omega = 0$ line; more on this will be detailed in § 5. For example, though one can actually see the existence of a secondary vortex for $Re = 5000$ in figure 6(*b*) at time $t = 0.9$ in the vicinity of $\theta = 45°$, the surface vorticity distribution graph in figure 14(*a*) suggests that the birth of this vortex actually takes place between $t = 0.80$ and 0.85. Likewise the several zones over which these secondary and tertiary vortex phenomena occur, their appearance, disappearance, symmetry (when the curve is plotted over the whole $0° \leqslant \theta \leqslant 360°$ range) and shift can also be better recognized from these curves. For example, the vorticity curves in figure 14(*b–d*) clearly depict the zones described in the schematic diagram of the vortex structures on the upper half of the cylinder in figure 5. Interestingly, at $t = 2.9$, one can see the simultaneous occurrence of sub-β-, sub-α- and α-phenomena leading to the formation of thirteen separation zones on the surface of the cylinder (see figure 6*i*). Multiple separation zones persist at subsequent times as well (figure 14*d*).

5. Structural bifurcation and unsteady flow separation

The predictions of the locations and the timings of the primary, secondary and tertiary vortex phenomena, and flow separation discussed in the previous sections were mainly based on qualitative observations. However, in order to establish accurate timings and precise locations of the separation points and the subsequent recirculation zones, more rigorous analytical tools are required.

The boundary layer separation theory proposed by Ghil *et al.* (2004, 2005) is based on the the structural bifurcation concept. As the two-dimensional incompressible viscous flow past an impulsively started circular cylinder also undergoes the process of bifurcation in its topological structure several times, it could prove to be a very efficient tool in predicting the exact location of the recirculation zones and precise time of their formation. Note that the newly developed theory has not so far been used to characterize the flow field associated with an impulsively started circular cylinder. We will endeavour to do this in order to have a detailed theoretical understanding of primary, secondary and tertiary vortex dynamics, and the interplay amongst them. The study of Ghil *et al.* (2004) showed the existence of an adverse pressure gradient in the neighbourhood of a bifurcation point (P^*, T^*) by utilizing the relation between vorticity and pressure in the solutions of the N–S equations and applying the Hopf Lemma (Evans 2002) for subharmonic functions. For a fluid flow governed by the N–S equations (2.1)–(2.2) with a no-slip boundary condition on the solid wall, the conditions for the separation of flow at a point P^* on the surface of a wall at time T^*

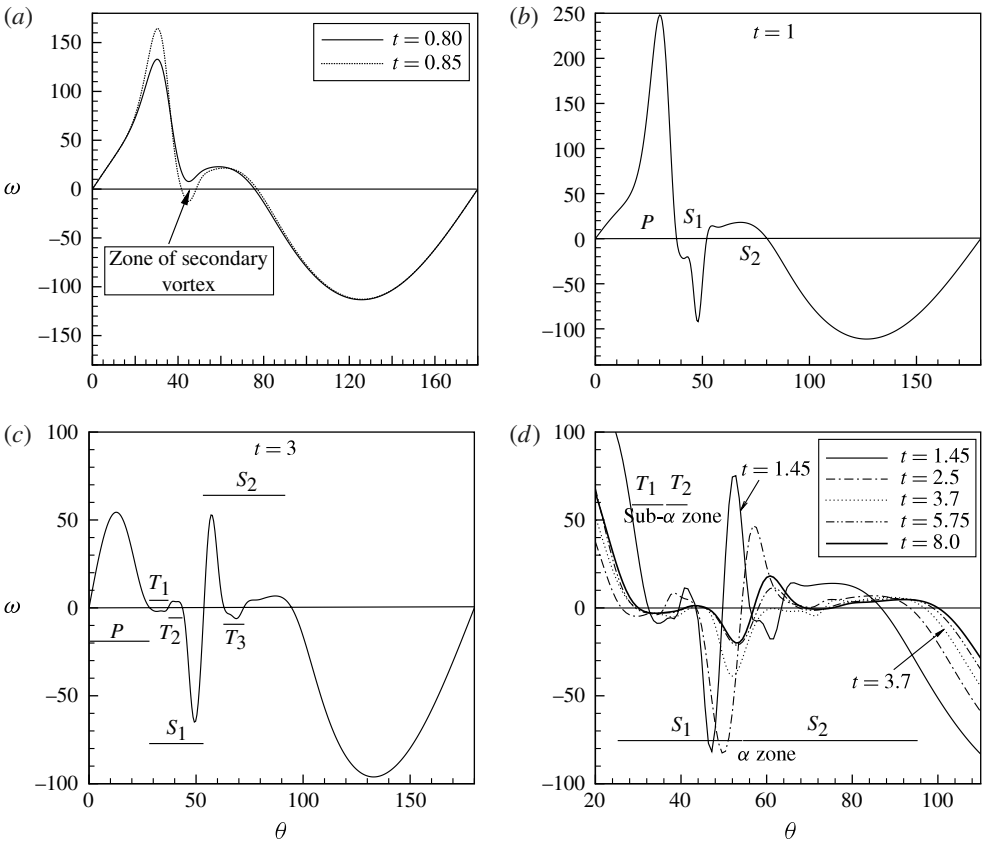

FIGURE 14. Vorticity distribution on the surface of the cylinder over several instants of time as shown on the figures, for $Re = 5000$.

are given as follows:

$$\omega(P^*, T^*) = 0, \quad \frac{\partial \omega}{\partial \tau}(P^*, T^*) = 0, \quad \frac{\partial^2 \omega}{\partial \tau^2}(P^*, T^*) > 0, \quad \frac{\partial \omega}{\partial t}(P^*, T^*) < 0, \quad (5.1)$$

where ω is the vorticity in (2.3), t the time, and τ is the direction tangential to the wall. It is assumed that a structural bifurcation occurs at time T^*, the normal derivative of the velocity field $\partial V/\partial n$ (n being the direction normal to the wall) has a degenerate singular point P^* on the wall and the shear flow is downward. When the flow is upward, the last two inequalities in (5.1) undergo change of signs. When (5.1) holds true:

(i) structural bifurcation occurs in the local structure of $\boldsymbol{V}$ at the boundary point P^* as t crosses T^*;

(ii) an adverse pressure gradient in the direction of the tangent to the surface is present at P^*.

Likewise, the high-Reynolds-number flow separation theory of Dommelen & Shen (1980) for an impulsively started circular cylinder, the boundary layer solutions by Peridier *et al.* (1991) and N–S simulations of Obabko & Cassel (2002) illustrate essentially the same phenomena in the flow induced by a vortex above a surface. Most

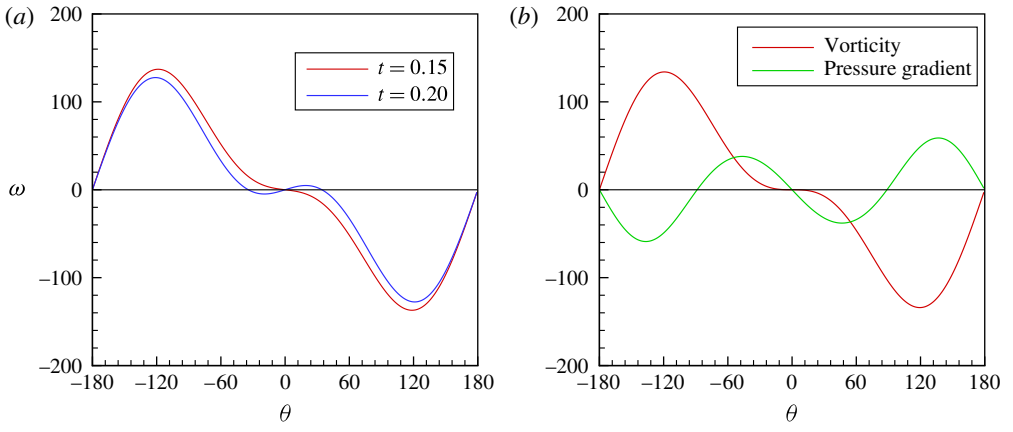

FIGURE 15. Distribution on the surface of the cylinder of (*a*) ω at times $t = 0.15$, 0.20 and (*b*) ω, p_θ at time $t = 0.1625$.

of the recent studies on the flow induced by a vortex above a surface are based on the theoretical description of unsteady separation resulting from the interaction between the viscous boundary layer and the outer inviscid flow (Cassel *et al.* 1996; Cassel 2000; Brinckmanand & Walker 2001; Obabko & Cassel 2002, 2005; Brinkerhoff 2011).

The following discussion pertains to the formation of the primary, secondary and tertiary vortices for $Re = 5000$ when they appear in the flow field for the first time.

5.1. *The first structural bifurcation*

In figure 15(*a*), we plot the vorticity distribution on the surface of the cylinder at time $t = 0.15$ and $t = 0.20$. Note that as the flow variables are periodic on the surface of the cylinder for $0 \leqslant \theta \leqslant 2\pi$, the θ range on the surface of the cylinder is shown as $-\pi \leqslant \theta \leqslant \pi$ so as to get a clear picture of the vorticity distribution in the neighbourhood of the point $(x, y) = (1, 0)$. This figure clearly indicates that no vortex is formed at time $t = 0.15$ while the vorticity curve crossing the zero vorticity line more than once is a clear indication of the formation of a recirculation zone on the surface at $t = 0.20$. In figure 16(*a*) we show the pair of symmetric vortices just formed behind the cylinder at time $t = 0.25$ by streamlines in the original (x, y) plane and while in figure 16(*b*) the streamtraces are plotted in the transformed (ξ, η) plane with a magnified ξ-axis in order to get a clear view of the vortices being formed and the direction of the flow. Following (5.1), while the formation of the primary recirculation zone on the upper half of the cylinder with a downward flow requires that ω has a local minimum at a degenerate singular point (P^*, T^*), ω must have a local maximum at such singular points for the formation of the primary recirculation zone at the lower half with an upward flow direction. Since the formation of the wake behind an impulsively started cylinder at moderately high Re starts with the inception of two symmetric recirculation zones at the same instant of time at $\theta = 0°$ (Bouard & Coutanceau 1980; Loc 1980; Coutanceau & Defaye 1991), the vorticity distribution curve on the surface of the cylinder at that particular instant must look like the one shown in figure 15(*b*), which is consistent with the observations made by Bakker (1989) and according to our computation is obtained at time $t = 0.1625$. As noted in earlier work (Bakker 1989) our observations also show that

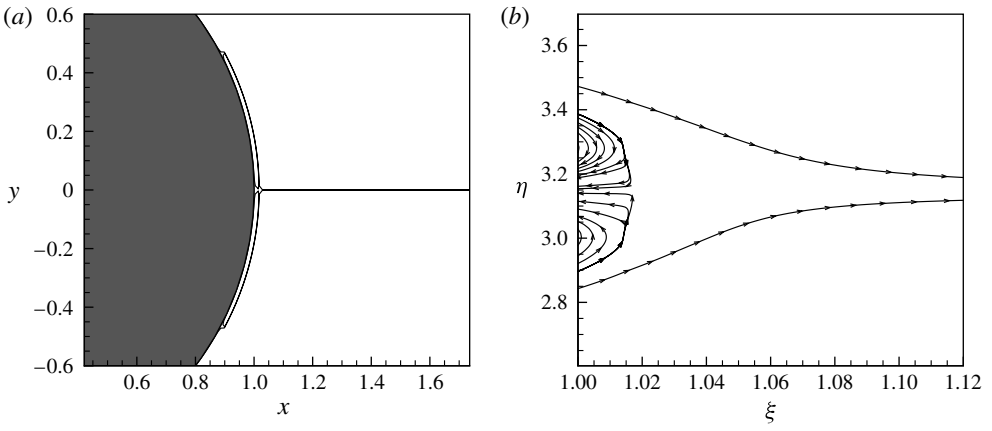

FIGURE 16. (*a*) Streamlines in the original (x, y) plane and (*b*) streamtraces in the (ξ, η) plane just behind the cylinder at time $t = 0.25$.

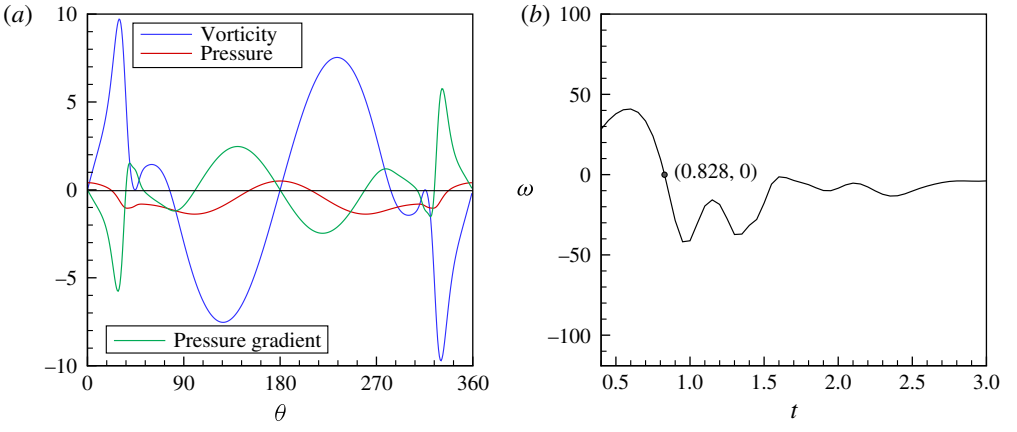

FIGURE 17. (*a*) Distribution of vorticity ω, pressure p and the pressure gradient p_θ along the surface of the cylinder at the time of the second structural bifurcation $t = 0.828$ and (*b*) time history of vorticity at the point $\theta = 44.8°$ on the cylinder surface.

point $(1, 0)$ is a hyperbolic saddle point (see Gurcan *et al.* 2005) and the pressure gradient p_θ along the wall will vanish there due to symmetry (figure 15*b*: p_θ is scaled up in order to make it comparable with ω).

5.2. *The second structural bifurcation*

As time goes on and as is obvious from figures 6(*a,b*) and 14(*a*), the secondary vortex is formed between $t = 0.80$ and 0.85. The primary vortices that had earlier formed behind the cylinder grow in size and strength which produces an adverse pressure gradient and thus leading the way for the formation of a secondary vortex (see figure 6*b*). In figure 17(*a*), we show the distribution of vorticity ω (which is scaled down in order to make it comparable with the pressure and pressure gradient), the pressure p and pressure gradient p_θ along the surface of the cylinder at time $t = 0.828$. It is clear from this figure that the vorticity reaches zero at $(\theta, t) = (44.8°, 0.828)$

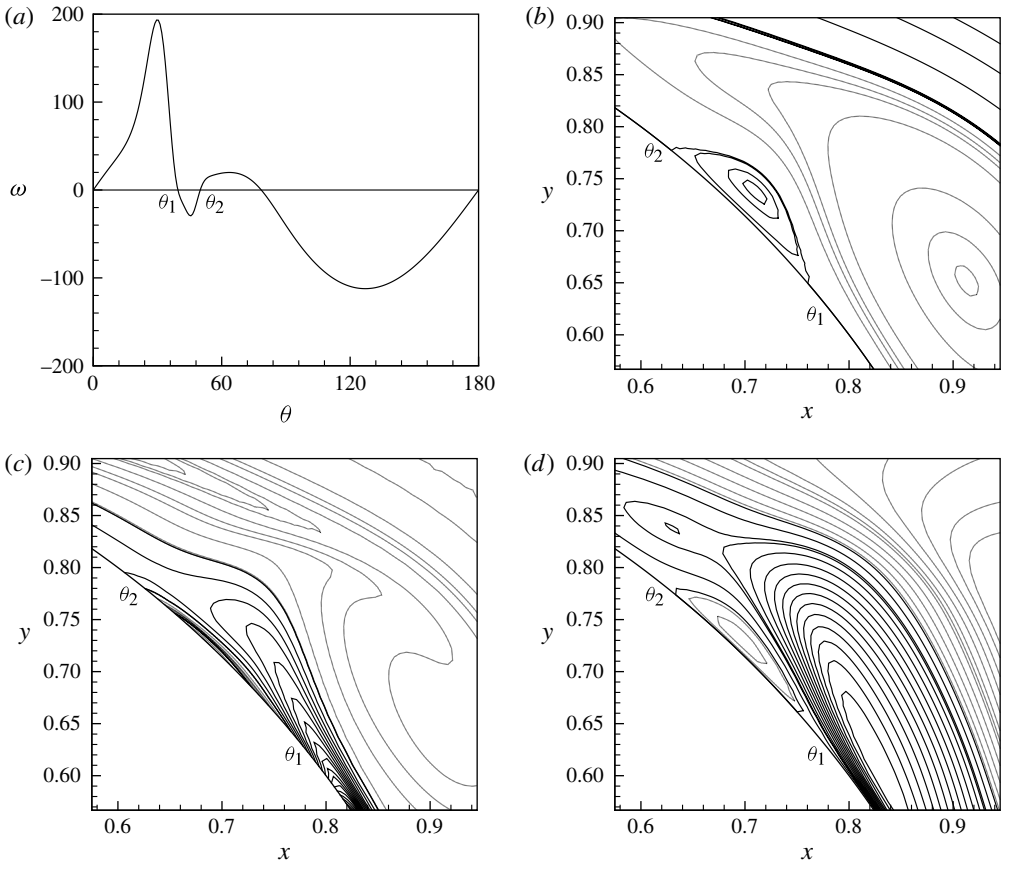

FIGURE 18. At time $t = 0.90$: (*a*) vorticity distribution on the surface of the cylinder, (*b*) streamfunction contours, (*c*) vorticity contours and (*d*) vertical velocity contours. In (*b–d*), the dotted lines denote contours with negative values.

as a local minimum in space and decreases in time, that is, $\omega(44.8°, 0.828) = 0$, $(\partial\omega/\partial\theta)(44.8°, 0.828) = 0$, $(\partial^2\omega/\partial\theta^2)(44.8°, 0.828) > 0$. In figure 17(*b*), we show the time history of the vorticity at the point $\theta = 44.8°$ on the surface; this figure clearly shows that $(\partial\omega/\partial t)(44.8°, 0.828) < 0$. Thus all the conditions given by (5.1) are satisfied, confirming that the second structural bifurcation occurs at time $t = 0.828$ at $\theta = 44.8°$ on the surface of the cylinder. When $t < 0.828$, there is no singular point for vorticity in the neighbourhood of $\theta = 44.8°$ as can be seen from figure 14(*a*) for $t = 0.80$ and the local structure of the streamfunction is as seen in figure 6(*a*). When $t = 0.828$, there is one degenerate singular point for vorticity at $\theta = 44.8°$ which decrease with time in the neighbourhood of $t = 0.828$ as seen in figure 17(*b*). When $t > 0.828$, one can see two isolated singular points $\theta_1 \approxeq 39.23°$ and $\theta_2 \approxeq 50.12°$ for vorticity on the solid surface as can be seen from figure 18(*a*) at time $t = 0.90$. The zoom plots of streamfunction and vorticity contours in figure 18(*b,c*) now clearly show the formation of the secondary recirculation zone. Likewise, the vertical velocity in figure 18(*d*) shows that the near-boundary flow is indeed reversed between θ_1 and θ_2.

The formation of this secondary vortex can also be explained in the light of viscous–inviscid interaction as outlined by Obabko & Cassel (2002). In order to

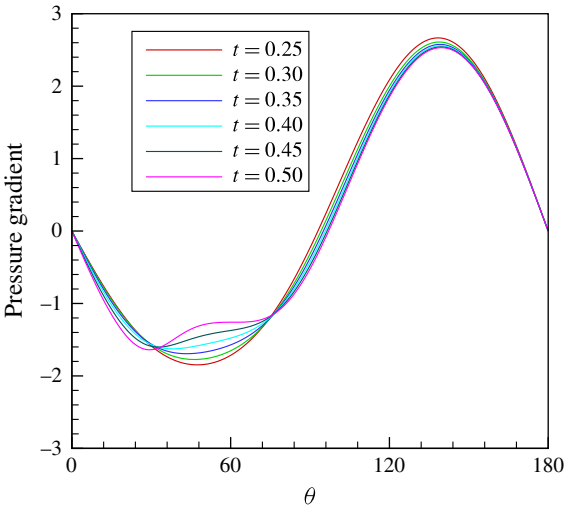

FIGURE 19. Pressure gradient p_θ along the surface of the cylinder for $0.25 \leqslant t \leqslant 0.50$.

determine when this viscous–inviscid interaction first begins, the pressure gradients in the direction of the cylinder surface are followed as time progresses. In figure 19, we plot p_θ on the surface of the cylinder in the time range $0.25 \leqslant t \leqslant 0.50$ at an interval of $\Delta t = 0.05$. One can clearly see that the pressure gradient begins changing in the vicinity of its minimum, where the streamlines abruptly change direction in order to pass over the recirculation region. Note that the region of this minimum pressure gradient is in the neighbourhood of $\theta = 44.8°$ where the second separation eventually occurs.

Obabko & Cassel (2002) defined unsteady separation as the onset of a finite time singularity from the point of view of unsteady boundary layer equations. According to them the formation of this singularity coincides with the onset of viscous–inviscid interaction. In the later stages, after the formation of the first recirculation zone, the boundary layer is concentrated in a narrow region that forms on the upstream side of the recirculation zone. Since the fluid particles at the separation point are rapidly compressed in the streamwise direction, they elongate in the direction normal to the wall. The elongation of the fluid particles in the normal direction leads to the growth of a sharp spike leading to what is called the spike formation. In figure 20(*a–d*), we track the development of the secondary vortices which finally leads to the so-called β-phenomenon. Here, in the left-hand column (i), we present combined streamfunction and vorticity contours at times $t = 0.45, 0.70, 0.80$ and 1.0 in the (r, θ) plane where the extent of the r scale has been reduced in order to show the evolution of the flow more clearly within the boundary layer, which is $O(Re^{-1/2})$. These plots are accompanied in column (ii) on the right by the corresponding vorticity, pressure and pressure gradient distributions along the surface of the cylinder. For a better view, the vorticity values are scaled down in order to bring them within the range of the pressure and pressure gradient.

It is known that the primary vortices formed at the rear of the cylinder produce a strong adverse pressure gradient (Koumoutsakos & Leonard 1995). As can be seen from figure 20(*ai*,*bi*), at time $t = 0.45$ the primary vortex grows in size normal to the surface in the r-direction and is moving upstream against the free stream. This leads to

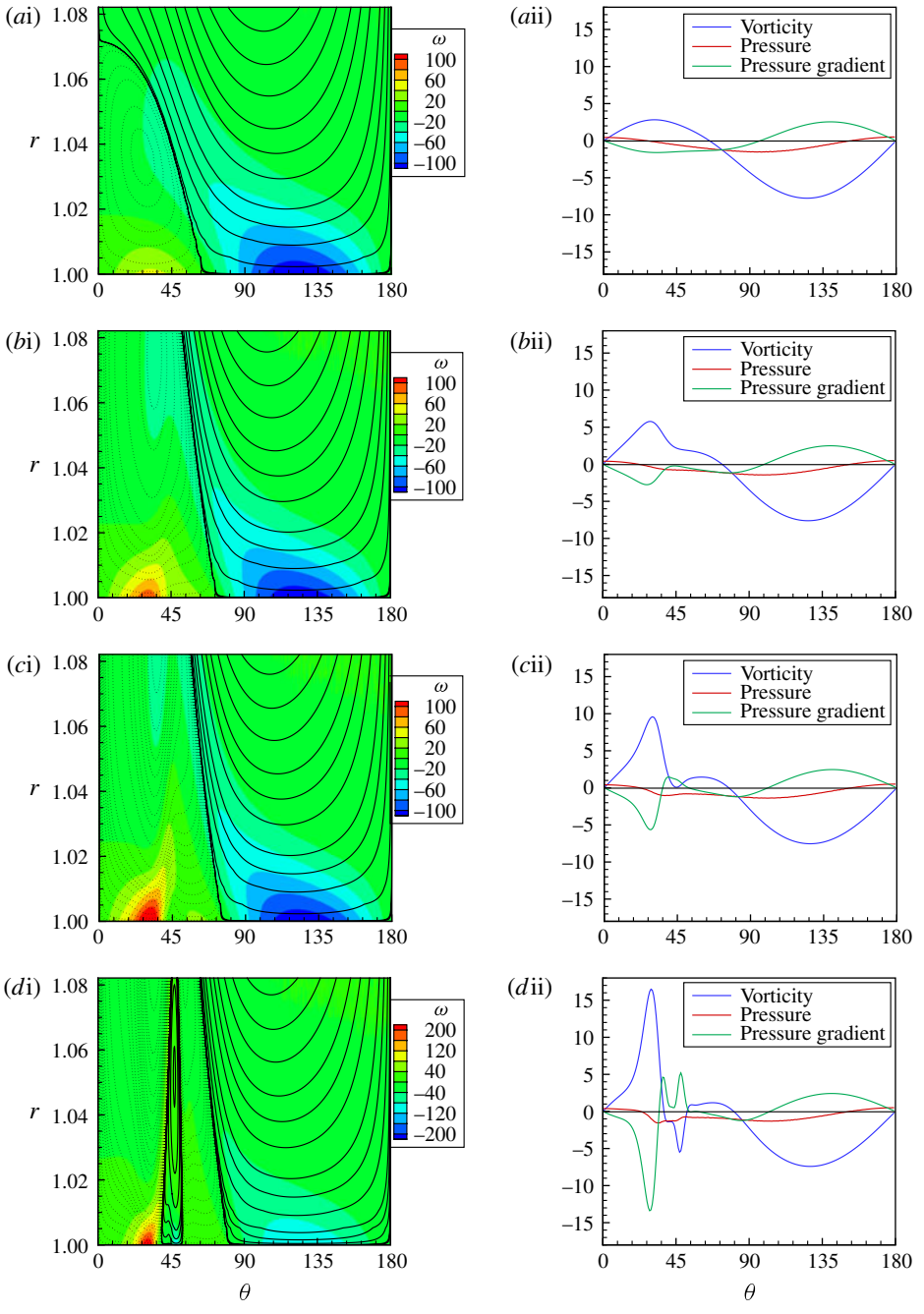

FIGURE 20. Combined streamfunction and vorticity contours (column i) and distribution of vorticity ω, pressure p and the pressure gradient p_θ along the surface of the cylinder (column ii) at times (*a*) $t = 0.45$, (*b*) $t = 0.70$, (*c*) $t = 0.80$ and (*d*) $t = 1.0$. Note that the streamlines are plotted using lines, with the dotted lines representing negative contour values, and the colour scale is used for plotting the vorticity contours.

changes in the pressure gradient p_θ in the vicinity of the primary vortex (figure 20*a*ii) which is more apparent in figure 20(*b*ii) at time $t = 0.70$ with the formation of a local maximum around $\theta = 44.8°$. The onset of viscous–inviscid interaction at this time leads to the formation of a very small spike (see the vorticity contours in figure 20*b*i) approximately around $\theta = 30°$ which grows normal to the surface in the r-direction. This can be clearly seen from the streamlines in figure 20(*c*i) at time $t = 0.80$ when the large-scale interaction has accelerated the spike formation process. At this time the pressure gradient exhibits a minimum at $\theta \approxeq 28.5°$ followed immediately by a local maximum at $\theta \approxeq 36°$ in the large-scale interaction region (see figure 20*c*ii). In this region, $p_\theta > 0$, which is locally adverse with respect to the flow beneath the recirculation region near to the surface. This rapid increase in p_θ in the near-wall flow direction causes the flow across the boundary layer to be compressed in the θ-direction. This results in an accelerated growth of the spike in the r-direction in the region of rapid change in pressure gradient. This eventually leads to the formation of the secondary vortex which is obvious from figure 20(*d*i) near $\theta = 44.8°$ at $t = 1.0$. This recirculation zone is also evident from the vorticity distribution on the surface around $\theta = 44.8°$ where one can see a small region of negative vorticity. We next proceed to document the formation of the tertiary vortex. The work of Koumoutsakos & Leonard (1995) indicated that the secondary vortices already present in turn will induce tertiary vortical regions on the surface of the cylinder. However, a clear depiction of the creation of tertiary structures could not be seen in their documentation.

5.3. *Formation of the tertiary vortex*

Next, we explain the formation of tertiary vortices T_2 and T_3 (refer to figure 5, the schematic diagram, and figure 6*e*, the streamlines at $t = 1.35$) with the help of figure 21 where we present combined streamline and vorticity contours, and the distribution of pressure gradient p_θ along the surface of the cylinder in the close range $0 \leqslant \theta \leqslant 90°$. As explained in figure 20(*d*), at time $t = 1.0$, the presence of the secondary vortex leads to the formation of a local minimum in p_θ at $\theta \approxeq 43.2^0$ (see figure 21*a*ii) which is analogous to the formation of a local maximum (but opposite in direction) in p_θ induced by the large-scale interaction that had led to the formation of the secondary vortex. In a similar way, the local minimum in p_θ caused by the secondary recirculation region becomes locally adverse, that is negative at $t = 1.35$ around $\theta \approxeq 45°$ (see figure 21*b*ii) and leads to the formation of the tertiary recirculation region T_2 near $\theta \approxeq 43.2°$. The same mechanism applies during the formation of the tertiary recirculation region T_3 around $\theta \approxeq 60°$ (see figure 21*b*i and figure 6*e*). The local maximum in p_θ at $\theta \approxeq 60°$ having a negative value (see the close up in figure 21*a*ii) become locally adverse at time $t = 1.35$ (see figure 21*b*ii) with a positive value and having a local maximum at $\theta \approxeq 60°$ where one can clearly see a tertiary recirculation zone (figure 21*b*i). The tertiary vortices T_2 and T_3 eventually lead to the sub-α-phenomenon in figure 10 and sub-β-phenomenon in figure 9 respectively.

In figure 22(*a*,*b*), we show the distribution of vorticity ω (which is scaled down again in order to make it comparable with pressure and pressure gradient), the pressure p and p_θ along the surface of the cylinder at time $t = 1.116$ and $t = 1.233$ respectively. These graphs correspond to the formation of tertiary vortices T_2 and T_3 described above. The corresponding time histories of the vorticity at $\theta = 43.2°$ and $\theta = 60°$ are shown in figure 23(*a*,*b*). Both figures 22 and 23 are consistent with the conditions given by (5.1). Note from figures 22(*a*) and 23(*a*) that vorticity at $\theta = 43.2°$ has a

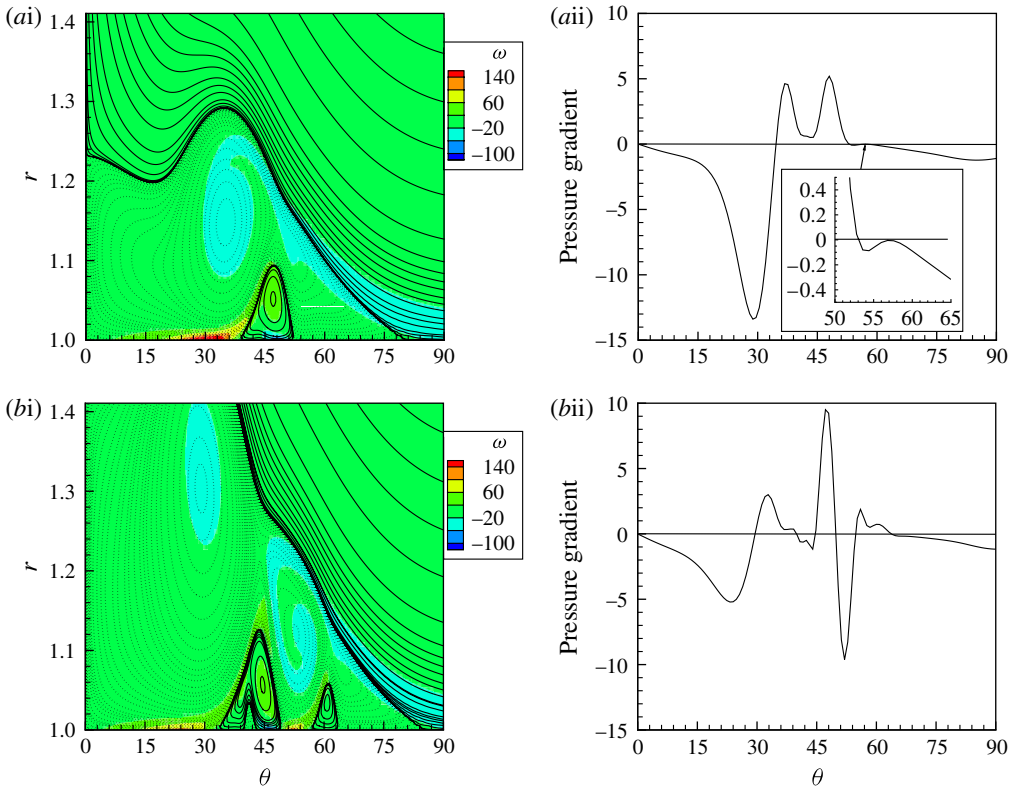

FIGURE 21. Combined streamfunction and vorticity contours (column i) and distribution of pressure gradient p_θ along the surface of the cylinder (column ii) at times (*a*) $t = 1.0$ and (*b*) $t = 1.35$.

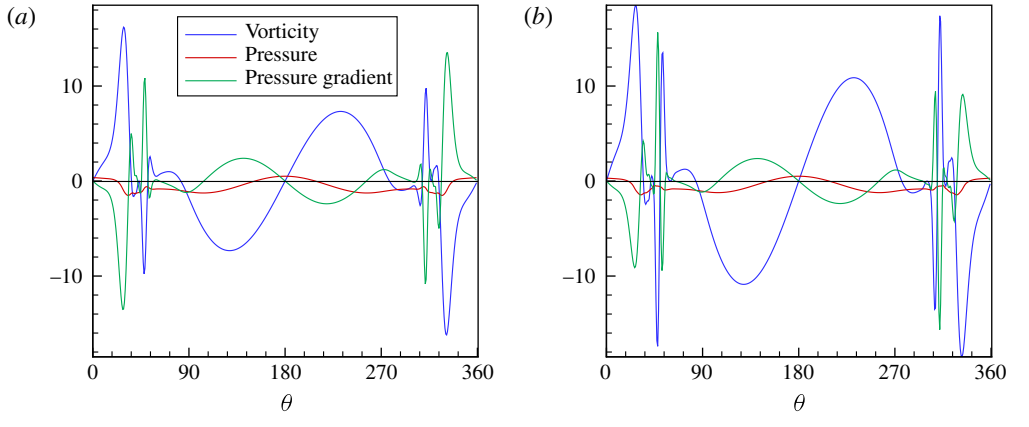

FIGURE 22. Distribution of vorticity ω, pressure p and the pressure gradient p_θ along the surface of the cylinder at the time of the formation of the tertiary vortices: (*a*) $t = 1.116$ and (*b*) $t = 1.233$.

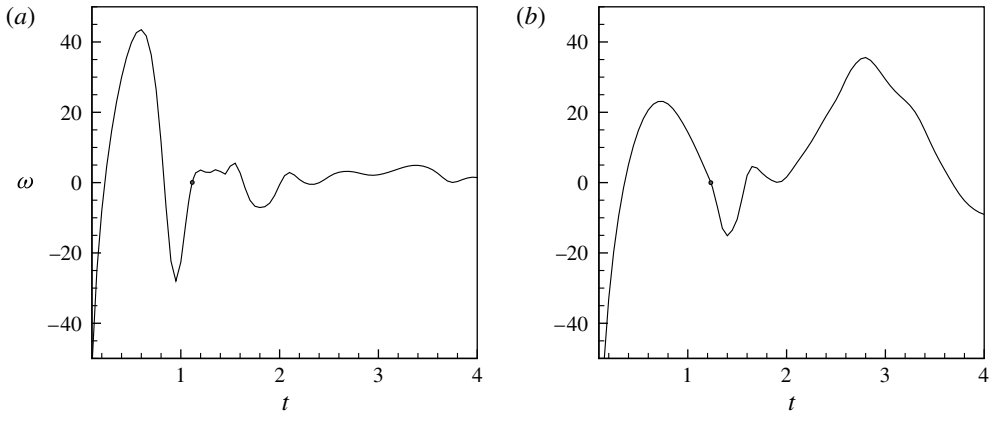

FIGURE 23. Time history of vorticity at the points (*a*) $\theta = 43.2°$ and (*b*) $\theta = 60°$ on the cylinder surface.

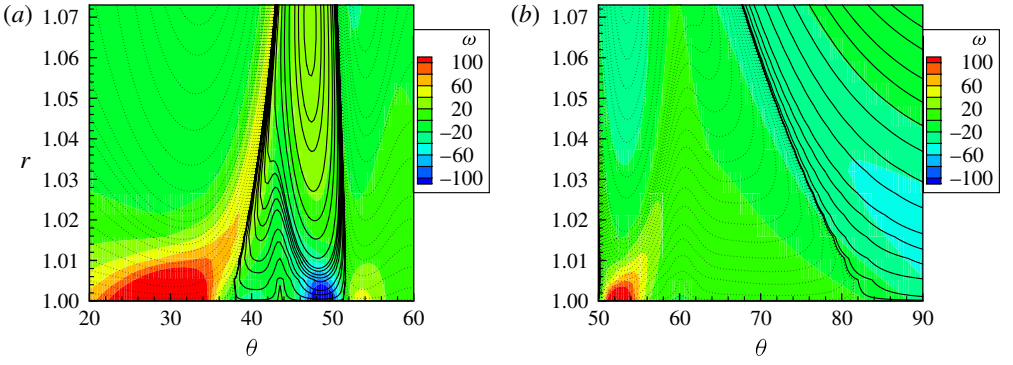

FIGURE 24. Combined streamfunction and vorticity contours showing spike formation before the separation leading to the tertiary vortices: (*a*) $t = 1.115$ at $\theta = 43.2°$ and (*b*) $t = 1.23$ at $\theta = 60°$.

local maximum and it is increasing with respect to time in the vicinity of $t = 1.116$. This is because of the reversal in the direction of the flow as opposed to those in figures 22(*b*), 23(*b*) and 17. Thus the third and fourth structural bifurcations which are accompanied by the formations of the tertiary vortices T_2 and T_3 occur at $(\theta, t) = (1.116, 43.2°)$ and $(1.233, 60°)$ respectively. Again the unsteady separation leading to the creation of the tertiary vortices is preceded by the spike formations as can be seen in figure 24(*a,b*) showing streamlines and vorticity contours, which is once again indicative of viscous–inviscid interaction.

Note that all our observations from our computations on the timings of the formation of the secondary and tertiary vortices and their location on the cylinder surface are consistent with the studies on boundary layer separation theory by Ghil *et al.* (2004) and the observations of Obabko & Cassel (2002) related to unsteady separation induced by a vortex.

6. Conclusion

In this study, we make an in-depth analysis of the intriguing structures that can be seen during α- and β-phenomena which are typical of the flow past an impulsively started circular cylinder at moderately high Reynolds numbers. The flow is computed by solving the biharmonic form of the Navier–Stokes equations using a recently developed compact finite difference scheme. In the process, we have also reported some tertiary vortex phenomena which we term sub-α and sub-β, which, to the best of our knowledge have not been reported earlier. We have shown that apart from occurring in isolation, sometimes the sub-α-phenomenon is preceded by the sub-β-phenomenon. Moreover, we have also reported a β-like phenomenon which closely resembles the β-phenomenon, but slightly differs in its formation. For the first time, the existence of these phenomena has been quantified by providing the strength of the vortices at different instants of time. Also, we have provided a new perception of the α-phenomenon by defining its existence in a strong and weak sense along with a clearer characterization of the β-phenomenon. The fascinating interplay between the secondary and tertiary vortices has been presented through the depiction of the distribution of vorticity and pressure gradient over the surface of the cylinder which also demonstrates the presence of several separation zones throughout the evolution of the flow.

Apart from the qualitative comparison, a detailed analysis has been carried on the topological structures of the primary, secondary and tertiary recirculation zones using the boundary layer separation theory based on the structural bifurcation concept. For the first time, using a recently developed theory a rigorous portrayal of transitions in the topological structure for the problem of flow past a circular cylinder has been presented.

We have also used the theory of unsteady flow separation which is based on the viscous–inviscid interaction to predict precisely the time of inception and the position of the recirculation zones. This has emphatically established the existence of tertiary vortices on the surface of the cylinder which eventually leads to the new tertiary phenomena reported by us. Our computation has revealed that for $800 \leqslant Re \leqslant 3000$, which was thought to be filled with the α-phenomenon in the early stages of the flow, the secondary vortices responsible for this phenomenon are never equivalent in strength; the α-phenomenon exists only in the weak sense from $Re = 1000$ onwards in this range. Likewise, contrary to some earlier studies reporting the α-phenomenon for $Re \geqslant 9500$ in the early stages, we cannot see the equivalence of the secondary vortices either in size or in strength. Interestingly, the range of Reynolds numbers $4000 \leqslant Re \leqslant 8000$ where the α-phenomenon is preceded by the β-phenomenon is also the range where the α-phenomenon exists in the strong sense. The secondary and tertiary vortex dynamics for even higher Reynolds numbers which is likely to reveal some more interesting features will be discussed in a separate paper in the near future.

REFERENCES

BAKKER, P. G. 1989 Bifurcation in flow patterns. PhD thesis, Technical University of Delft, Netherlands.

BEN-ARTZI, M., CROISILLE, J. P. & FISHELOV, D. 2006 Convergence of a compact scheme for the pure streamfunction formulation of the unsteady Navier–Stokes system. *SIAM J. Numer. Anal.* **44**, 1997–2024.

BEN-ARTZI, M., CROISILLE, J. P., FISHELOV, D. & TRACHTENBERG, S. 2005 A pure-compact scheme for the streamfunction formulation of Navier–Stokes equations. *J. Comput. Phys.* **205**, 640–664.

BOUARD, R. & COUTANCEAU, M. 1980 The early stage of development of the wake behind an impulsively started cylinder for $40 \leqslant Re \leqslant 10^4$. *J. Fluid Mech.* **101**, 583–607.

BRINCKMANAND, K. W. & WALKER, J. D. A. 2001 Instability in a viscous flow driven by streamwise vortices. *J. Fluid Mech.* **432**, 127–166.

BRINKERHOFF, J. R. 2011 Interaction of viscous and inviscid instability modes in separation-bubble transition. *Phys. Fluids* **23**, 124102.

CASSEL, K. W. 2000 A comparison of Navier–Stokes solutions with the theoretical description of unsteady separation. *Phil. Trans. R. Soc. Lond.* A **358**, 3207–3227.

CASSEL, K. W., SMITH, F. T. & WALKER, J. D. 1996 The onset of instability in unsteady boundary-layer separation. *J. Fluid Mech.* **315**, 223–256.

CHANG, C.-C. & CHERN, R.-L. 1991 A numerical study of flow around an impulsively started circular cylinder by a deterministic vortex method. *J. Fluid Mech.* **233**, 243–263.

CHOU, M.-H. & HUANG, W. 1996 Numerical study of high-Reynolds-number flow past a bluff object. *Intl J. Numer. Meth. Fluids* **23**, 711–732.

COUTANCEAU, M. & DEFAYE, J.-R. 1991 Circular cylinder wake configurations: a flow visualization survey. *Appl. Mech. Rev.* **44**, 255–305.

DOMMELEN, L. L. & SHEN, S. F. 1980 The spontaneous generation of the singularity in a separating laminar boundary layer. *J. Comput. Phys.* **38**, 125–140.

EVANS, L. C. 2002 *Partial Differential Equations*. American Mathematical Society.

GHIL, M., LIU, J. G., WANG, C. & WANG, S. 2004 Boundary-layer separation and adverse pressure gradient for 2-D viscous incompressible flow. *Physica* D **197**, 149–173.

GHIL, M., MA, T. & WANG, S. 2005 Structural bifurcation of 2-d nondivergent flows with Dirichlet boundary conditions applications to boundary-layer separation. *SIAM J. Appl. Maths* **65**, 1576–1596.

GOODRICH, J. W. & SOX, W. Y. 1989 Time-dependent viscous incompressible Navier–Stokes equations: the finite difference Galerkin formulation and streamfunction algorithms. *J. Comput. Phys.* **84**, 207–241.

GUPTA, M. M. & KALITA, J. C. 2005 A new paradigm for solving Navier–Stokes equations: streamfunction-velocity formulation. *J. Comput. Phys.* **207**, 52–68.

GURCAN, F., DELICEOGLU, A. & BAKKER, P. G. 2005 Streamline topologies near a non-simple degenerate critical point close to a stationary wall using normal forms. *J. Fluid Mech.* **539**, 299–311.

KALITA, J. C. & GUPTA, M. M. 2010 A streamfunction-velocity approach for the 2D transient incompressible viscous flows. *Intl J. Numer. Meth. Fluids* **62**, 237–266.

KALITA, J. C. & RAY, R. K. 2009 A transformation-free hoc scheme for incompressible viscous flows past an impulsively started circular cylinder. *J. Comput. Phys.* **228**, 5207–5236.

KALITA, J. C. & SEN, S. 2012*a* The biharmonic approach for unsteady flow past an impulsively started circular cylinder. *Commun. Comput. Phys.* **12**, 1163–1182.

KALITA, J. C. & SEN, S. 2012*b* Triggering asymmetry for flow past circular cylinder at low Reynolds numbers. *Comput. Fluids* **59**, 44–60.

KOUMOUTSAKOS, P. & LEONARD, A. 1995 High-resolution simulations of the flow around an impulsively started cylinder using vortex methods. *J. Fluid Mech.* **296**, 1–38.

KUPFERMAN, R. 2001 A central difference scheme for a pure streamfunction formulation of incompressible viscous flow. *SIAM J. Sci. Comput.* **23**, 1–18.

LOC, T. P. 1980 Numerical analysis of unsteady secondary vortices generated by an impulsively started circular cylinder. *J. Fluid Mech.* **100**, 111–128.

LOC, T. P. & BOUARD, R. 1985 Numerical solution of the early stage of the unsteady viscous flow around a circular cylinder: a comparison with experimental visualization and measurements. *J. Fluid Mech.* **160**, 93–117.

MA, T. & WANG, S. 2002 Topology of 2D incompressible flows and applications to geophysical fluid dynamics. *RACSAM, Rev. R. Acad. Cien. A Mat.* **96**, 447–459.

OBABKO, A. V. & CASSEL, K. W. 2002 Navier–Stokes solutions of unsteady separation induced by a vortex. *J. Fluid Mech.* **465**, 99–130.

OBABKO, A. V. & CASSEL, K. W. 2005 On the ejection-induced instability in Navier–Stokes solutions of unsteady separation. *Phil. Trans. R. Soc. Lond.* A **363**, 1189–1198.

PERIDIER, V. J., SMITH, F. T. & WALKER, J. D. A. 1991 Vortex-induced boundary-layer separation. Part 1. The unsteady limit problem $Re \to \infty$. *J. Fluid Mech.* **232**, 99–131.

SANYASIRAJU, Y. V. S. S. & MANJULA, V. 2005 Flow past an impulsively started circular cylinder using a higher-order semi compact scheme. *Phys. Rev.* E **72**, 1–10.

SARPKAYA, T. & SCHOAFFT, R. L. 1979 Inviscid model of two-dimensional vortex shedding by a circular cylinder. *AIAA J.* **17**, 1193–1200.

SENGUPTA, T. K. & SENGUPTA, R. 1994 Flow past an impulsively started circular cylinder at high Reynolds number. *Comput. Mech.* **14**, 298–310.

SINGH, S. P. & MITTAL, S. 2004 Energy spectra of flow past a circular cylinder. *Intl J. Comput. Fluid Dyn.* **18**, 671–679.

STEPHENSON, J. W. 1984 Single cell discretization of order two and four for biharmonic problems. *J. Comput. Phys.* **55**, 65–80.

THOMAN, D. C. & SZEWCZYK, A. A. 1969 Time-dependent viscous flow over a circular cylinder. *Phys. Fluids Suppl.* II **12**, 76–86.